A Model for Simulating the Flow of Fluid Through a Microcantilever Sensor Cell

by

© **Colby Morgan**

A thesis submitted to the School of Graduate
Studies in partial fulfillment of the requirements for
the degree of Bachelor of Science (Honours).

Department of Physics & Physical Oceanography
Memorial University

February 2020

St. John's, Newfoundland and Labrador, Canada

Abstract

Microcantilever sensors are highly sensitive detectors capable of detecting target chemicals in solutions with concentrations in the parts per billion. Commercial and custom built sensor-based instruments make use of one or more probes consisting of eight cantilevers each. Until now the cantilevers have been treated equally, however, since they are in different locations with respect to the flow of input target chemicals this might not be the case. It is important to understand the concentration of targets in the vicinity of each cantilever to see what concentration each cantilever actually experiences. In this work we developed a model to simulate fluid motion throughout the cantilever sensor cell. It was found that there is a lot of variability in the flow across the cantilevers, which is suspected to impact the absorption rate. In accordance with the flow, there are regions of high and low pressure on the surface of the cantilevers, which could result in misleading deflection readings. Understanding the fluid motion is the first step towards properly understanding the deflection signal of each cantilever.

Table of Contents

List of Figures

Nomenclature

Physical Constants

p_A	Atmospheric Pressure:	101.3 kPa
N_A	Avogadro's Number:	6.023×10^{23} mol^{-1}
k_B	Boltzmann's Constant:	1.38065×10^{-23} kg m^2 s^{-2} K^{-1}
g	Gravitational Acceleration (Earth's Surface):	9.807 m s^{-2}
R	Universal Gas Constant:	8.3145 J K^{-1} mol^{-1}

Symbols

$\mathbf{\Omega}$	Domain
$\partial\mathbf{\Omega}$	Boundary of Domain
$\overleftrightarrow{\sigma}$	Stress Tensor
σ_{ij}	Normal Stress
τ_{ij}	Shearing Stress
$\mathbf{S}$,S_{ij}	Strain Rate Tensor
V	Constant Volume
μ	Dynamic Viscosity
$\mathbf{f}$	Force Per Unit Volume
δ_{ij}	Kronecker Delta Function
ρ	Mass Density
$\mathbf{x}$	Position Vector
$\mathbf{e}_i$	Unit Vector In The i-Direction

Acronyms

CFD Computational Fluid Dynamics

CSG Constructive Solid Geometry

FEA Finite Element Analysis

FSI Fluid Structure Interaction

IPCS Incremental Pressure Correction Scheme

NS Navier-Stokes

PDE Partial Differential Equation

PSD Position Sensitive Detector

Chapter 1

Introduction & Background

1.1 Microcantilever Sensors

Microcantilever sensors are chemically activated micromachined beams fixed at one end and free at the other that can be used to perform ultra-sensitive measurements of various physical and chemical phenomena. They are typically fabricated from silicon and are hundreds of micrometers long, around 30-50 micrometers wide, and less than 1 μm thick. A thin film of gold, approximately 20 nm thick, is applied to the top of the microcantilever which provides a better interface for attaching chemical functional groups. This surface is then rendered chemically active by coating it with a receptive layer that is capable of binding with target molecules in the solution. A simplified schematic of the microcantilever sensor viewed from the side is shown in Figure 1.1.

Figure 1.1: Schematic drawing of a single microcantilever viewed from the side. It consists of three layers: a silicon cantilever of precise geometry, a thin gold film, and a functional group that was synthesized to react with desired target molecules.

Microantilever sensors are now more commonly fabricated in arrays of eight cantilevers on a single chip (Figure 1.2). This allows for the simultaneous execution of eight sensing experiments. Depending on the nature of the target, one type of receptive layer may be more suitable than another; it is common to include a variety of cantilevers, each seeking a specific target, to broaden the applicability of the setup. Furthermore, to increase the reliability of each measurement, it is sometimes desirable to include several cantilevers each coated with the same receptors thereby decreasing the likelihood of false positives.

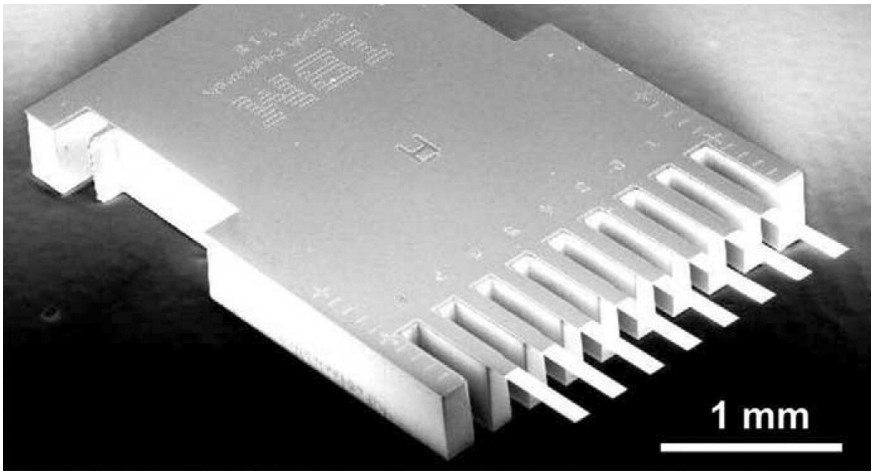

Figure 1.2: Scanning electron micrograph of a microcantilever sensor array. Image used with permission from [9]. Credit: Viola Barwich, University of Basel, Switzerland.

1.1.1 Method of Operation

Microcantilever sensors provide quantitative measurements of the concentration of target chemicals in a gas or liquid environment. They operate in either static mode, or dynamic mode [8]. In static mode, target molecules in solution bind with the receptive layer of the cantilever inducing a surface stress causing the cantilever to bend. The extent by which it deflects is measured using an optical beam deflection system[6] (Figure 1.4) and quantitative measurements are drawn. In dynamic mode, the cantilever is made to oscillate at one of its resonant frequencies using a piezoelectric actuator. As the chemical receptors on the cantilever adsorb target species it deposits mass which in turn changes the resonant frequency, which is sufficient information to calculate the added mass.

1.2 Experimental

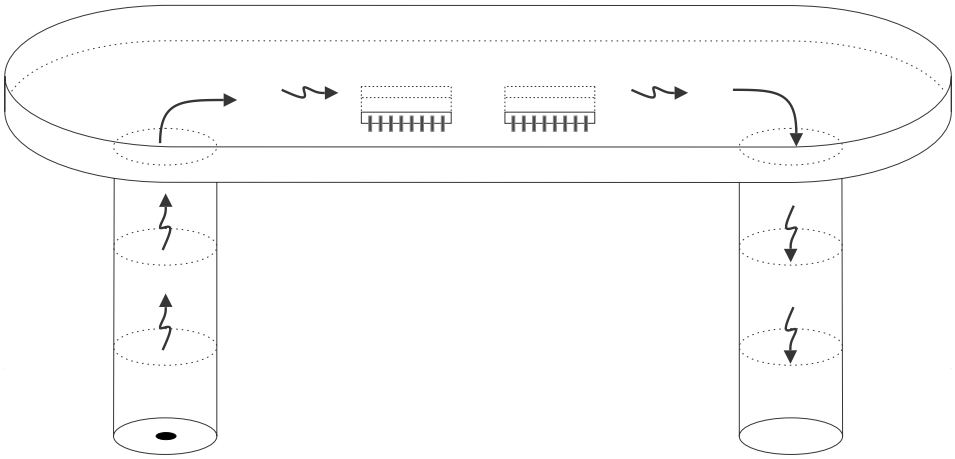

Figure 1.3: Idealized schematic of the experimental setup.

A schematic of the 16-cantilever setup used in our research group is illustrated in Figure 1.3. The cantilevers operate in static mode, and the extent of their deflection is measured using a laser and a Position Sensitive Detector (PSD) as in Figure 1.4. To minimize the amount of noise in the readings, the deflection is reported relative to one of the eight cantilevers per array (the reference cantilever). This cantilever is similar to the rest but is non-receptive to the target chemicals in the solution. Prior to the experimentation, the system is brought to thermal equilibrium by flowing research-grade distilled water through it. After a few minutes a chemical analyte is injected at the inlet, allowing it to run through the system, and the response of each cantilever is monitored and recorded over time.

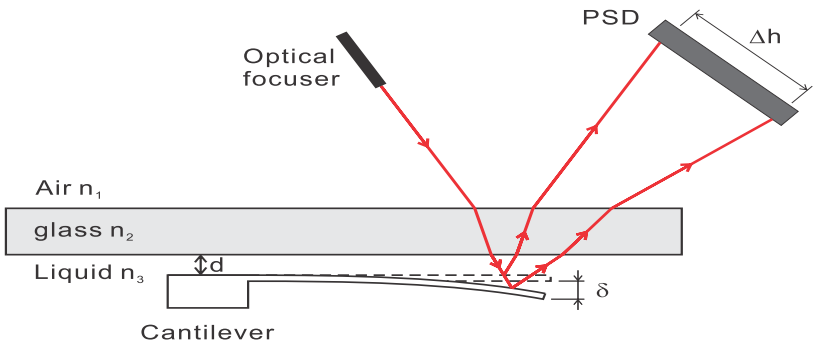

Figure 1.4: Diagram of the optical beam deflection system used in our research group. The position at which the beam hits the PSD is used to measure the extent of the cantilever deflection. Drawing courtesy of Dr. Luc Beaulieu, Memorial University of Newfoundland.

1.3 Motivation

Chemicals are introduced to the cantilevers by means of fluid transport. With reference to Figure 1.3, the chemicals move up the inlet pipe, to the right over the cantilevers, and down through the outlet pipe where they exit the cell. Considering the geometry of the system, it is expected that the fluid motion will be very complex with preferential pathways for bulk transport. Consequently, this means that chemicals will be advected unevenly through the cell, and the concentration of target species could vary considerably across the cantilevers. Additionally, the adsorption of target species onto the cantilever surface will decrease the concentration of the surrounding solution, which could potentially effect neighbouring cantilevers. The aim of this work is to investigate the flow using the methods of computational fluid dynamics. This provides the foundation needed to model more sophisticated problems such as the transport of chemicals by advection and diffusion or the bending and twisting of the cantilevers due to fluid motion.

Questions

In general, the long term objective is to gain a better understanding of cantilever sensor measurements which can be used to further optimize the setup by increasing detection limits, reproducibility, and reliability. This work was conducted with the following questions in mind:

1. What happens to the solution as it flows across the cantilevers? Does the flow of the solution remain laminar or does it become turbulent?

2. What is the relative detection of each of the cantilevers on the chip based on their position relative to the solution stream? Do cantilevers upstream detect more particles then the cantilevers downstream due to depletion? How is this relationship affected by the concentration of the target?

3. What is the relationship between the solution flow rate and the detection of the targets? If the flow is too high the detection rate presumably decreases because the attractive force between the cantilever and the targets is not strong enough to alter the path of the targets in the solution.

Although it is not explored in this thesis, there are many questions surrounding chemical absorption by the microcantilevers. None of which can be answered without first understanding the complex flow of particles inside the setup. This will be the primary objective of the thesis—to fully elucidate the dynamics of fluid in the experimental setup.

Assumptions

The real physical system is very complicated. In order to make any progress with a numerical model, the following simplifications are made:

1. The system is isothermal.
2. The fluid is well behaved and incompressible; properties such as viscosity are constant and do not depend on applied forces (Exemplar of a Newtonian fluid).
3. The cantilevers are rigid and do not bend. This restraint was made simply in the interest of saving computing time. This assumption can be removed later when resources permit, allowing for the dynamic simulation of fluid flow coupled with the bending and twisting of the cantilevers.

1.4 Objective & Methodology

In this thesis Computational Fluid Dynamics (CFD) is employed to study the flow responsible for transporting target molecules in solution across the arrays of microcantilevers. The method of Finite Element Analysis (FEA) (section 3.2) is used to solve the Navier-Stokes (NS) equations (section 2.6) numerically. This method discretizes the entire fluid volume (the domain) into many small elements (tetrahedrons in this case) constructing what is known as the mesh (section 3.4). Just like the domain, the equations must also be discretized. There are a number of methods for discretizing the Navier-Stokes equation. The one used here is a modified version of Chorin's method (section 3.3.1) known as the Incremental Pressure Correction Scheme (IPCS). It serves as an alternative to directly solving a nonlinear Partial Differential Equation (PDE), and it allows for the pressure and velocity to be decoupled and solved independently.

1.5 Scope & Outline

The focus of this thesis will be on the fluid dynamics. The objective and questions to be answered have already been discussed. In Chapter 2, the theory[I] and mathematics necessary to approach this problem is formalized. Starting from the general conservation laws, and making a number of arguments valid for this problem, we arrive at a simplified variant of the well known NS equations. Chapter 3 provides a technique of utilizing these equations by discretizing them both spatially and temporally, and solving them numerically using the method of FEA. In Chapter 4, the general equations and methods developed previously are consolidated and readdressed with all the information necessary to solve for the flow through the cantilever setup. In this chapter all of the results are presented and critiqued, and the validity of the numerical solution is justified. Finally, in Chapter 5, the thesis is summarized and conclusions are drawn, leaving off with a short word on intentions for future work.

[I] While the intention was to make this a standalone document, the breadth of knowledge required to cover the theory of fluid dynamics and finite element methods is far too substantial for a thesis. The reader is directed to the bibliography for supplementary material. It is also advised that the reader familiarize themselves with the appendix material, especially when it is referenced in-text.

Chapter 2

Theory & Mathematics

The fundamental principles governing fluid dynamics are the conservation laws for mass, momentum, and energy. They may be defined in either differential form, useful in the particle description, or extended into integral form which applies to larger bodies. Both are valid, although one may be more favourable in some situations. In this thesis, the equations are derived from an intuitive control-volume[I] approach, which is most naturally written in integral form. The result is later cast into differential form with help from the divergence theorem.

Before attempting to derive the equations governing fluid motion it is necessary to choose a reference frame [II]. There are two choices: either a Lagrangian frame, which traces the trajectory of fluid particles, or an Eulerian frame that observes fluid passing through a fixed location. In practice, the Eulerian specification is more suitable, however it is far more complicated mathematically. The approach presented in this chapter develops the mathematics from the simpler Lagrangian reference frame and then applies the adjustments needed to change frames. Fortunately, converting between reference frames is not such a daunting task with an understanding of the Material Derivative (Section: A.2).

[I] A control-volume is a fictitious volume that is used to study fluid motion in a particular region. Depending on the choice of reference frame (see section A.1) this volume could move with a parcel of fluid, tracing its motion, or remain fixed in space and observe how fluid passes through it.

[II] It is recommended to read Appendix section A.1 before proceeding in this discussion.

2.1 Continuum Hypothesis

Fluid dynamics is the macroscopic study of fluid in motion. Properties such as density, pressure, and velocity that are normally defined on the basis of interacting molecules are now averaged quantities which vary smoothly over the domain[III]. These averaged properties are now referred to as fields, which are simply functions of space and time. The advantage of describing properties using fields is that it can be evaluated at every single point in the domain; before averaging, the density (mass/volume) at a point of zero volume would be undefined. In the continuum sense, a point is just a very small element of finite volume with constant (averaged) fluid properties. This can be mathematically well-defined in terms of a limit as the fluid elements can be made infinitesimally small. Physically, the continuum hypothesis assumes that these fluid elements, even though they can be very small, are still much larger the size of the individual molecules that make up the fluid. The idea of a fluid element is very meaningful in fluid dynamics, especially when it comes to numerical simulation. This will be discussed more in Chapter 3.

[III]The domain is entire space where fluid exists.

2.2 Reynolds Transport Theorem

The equations of fluid dynamics can be derived from conservation laws for mass, momentum, and energy. All of which are unified by one generalized equation—the Reynolds Transport Theorem. This theorem describes how functions change in the presence of a dynamic fluid medium. It is instrumental in answering questions like: how does fluid motion effect the transport of mass, momentum, and energy? A useful attribute of this theorem is that it automatically takes care of the adjustments needed in converting between reference frames. Mathematically, this theorem provides a means of bringing the differential operator inside the integral using the relation,

$$\frac{d}{dt}\int_{\Omega(t)} F(\vec{\mathbf{x}},t)\; dV = \int_{\Omega(t)} \frac{\partial F\left(\vec{\mathbf{x}},t\right)}{\partial t}\; dV + \int_{\partial\Omega(t)} F\left(\vec{\mathbf{x}},t\right)\; \vec{\mathbf{b}}\cdot\hat{\mathbf{n}}\; dA. \tag{2.1}$$

The Reynolds Transport Theorem is most easily understood from a graphical perspective. Suppose we wish to study a property such a mass, enthalpy, or kinetic energy represented by the scalar function $F(\vec{\mathbf{x}},t)$. Following the Lagrangian specification, a parcel[IV] of fluid, with volume $\Omega(t)$, is enclosed by the surface $\partial\Omega(t)$. Note that the volume is dynamically changing with time. Therefore, bringing the derivative inside of the integral requires knowledge of how the volume is transforming. The resolution comes from the realization that any change in volume $\Delta\Omega$ originates from the displacement of the boundary, resulting in the surface integral on the RHS of the equation (Eq. 2.1). In an infinitesimal amount of time Δt an element of the surface dA, moving with velocity $\vec{\mathbf{b}}$, sweeps out the volume $(\vec{\mathbf{b}}\Delta t)\cdot\hat{\mathbf{n}}\; dA$.

[IV] It is common language in fluid dynamics to refer to a small amount of fluid, that is identified from the rest, as a parcel. It is allowed to distort its shape with the flow, but its mass must remain constant.

2.3 Conservation of Mass

Mass can be neither created nor destroyed. As with many equations in fluid dynamics this statement is written in terms of an intensive variable that is characteristic of the type of fluid, in this case the density ρ. The conservation of mass is stated as,

$$\frac{d}{dt}\int_{\Omega(t)} \rho(\vec{\mathbf{x}},t)\; dV = 0. \tag{2.2}$$

A volume element within a fluid moves and deforms so that it always contains the same mass. This implies that the boundary of the volume must move with the local velocity $\vec{\mathbf{u}}$ of the fluid. Following from the Reynolds Transport Theorem (2.2) with $\vec{\mathbf{b}} = \vec{\mathbf{u}}$ and $F = \rho$,

$$\int_{\Omega(t)} \frac{\partial \rho\left(\vec{\mathbf{x}},t\right)}{\partial t}\; dV + \int_{\partial\Omega(t)} \rho\left(\vec{\mathbf{x}},t\right)\vec{\mathbf{u}}\left(\vec{\mathbf{x}},t\right)\cdot\hat{\mathbf{n}}\; dA = 0. \tag{2.3}$$

Together the volume and surface integral above explain how the mass moves and deforms with the fluid motion $\vec{\mathbf{u}}$. Applying the divergence theorem to the second term allows this expression to be written under one integral. In order to vanish for all $\Omega(t)$, the integrand must be zero, leading to the *continuity* equation:

$$\frac{\partial \rho(\mathbf{x},t)}{\partial t} + \nabla\cdot\left(\rho(\mathbf{x},t)\;\vec{\mathbf{u}}(\mathbf{x},t)\right) = 0 \tag{2.4}$$

Observe that when ρ is constant in space and time, then (Eq. 2.4) reduces to reduces to $\nabla\cdot\vec{\mathbf{u}} = 0$. This is well known in fluid dynamics as the *incompressibility condition*. While ρ was assumed to be constant to get this result, in reverse, the incompressibility condition says that density does not change with pressure. This condition is paramount in solving some PDE's both analytically and numerically. This simplification is justifiable for most liquids which are nearly incompressible under standard conditions [V], and even some gases for low flow speeds [7, p. 113].

Making use of the *material* vector identity $\nabla\cdot(\rho\mathbf{u}) = \rho\nabla\cdot\mathbf{u} + (\mathbf{u}\cdot\nabla)\rho$ and the material derivative (Eq. A.1), the continuity equation (Eq. 2.4) can be rewritten as

$$\frac{\partial\rho}{\partial t} + \vec{\mathbf{u}}\cdot\nabla\rho + \rho\nabla\cdot\vec{\mathbf{u}} = \frac{D\rho}{Dt} + \rho\nabla\cdot\vec{\mathbf{u}} = 0 \tag{2.5}$$

[V] Atmospheric temperature and pressure.

2.4 Conservation of Momentum

Consider a volume $\Omega(t)$ enclosed by the surface $\partial\Omega(t)$ moving with the fluid. The forces applied to the mass are governed by Newtons 2$^{\text{nd}}$ law $\mathbf{F} = m(t)\mathbf{a}(t)$. Where mass is constant in the Lagrangian reference and $\mathbf{F} = m\frac{d\mathbf{u}}{dt}$. Dividing by the volume of the parcel $\Omega(t)$ so that only the intensive variable, density ρ, is involved, and replacing the differential with the material derivative (Eq. A.1) required in the Eulerian frame gives the force per unit volume, $\mathbf{f}$[VI]:

$$\rho\frac{D\mathbf{v}}{Dt} = \mathbf{f}_{\text{Net}} = \mathbf{f} + \mathbf{f}_{\text{surface}}.$$

Body forces $\mathbf{f}$ are due to external agents such a magnetic or gravitational fields, and can be written as $\mathbf{f} = \rho\mathbf{g}$, where $\mathbf{g}$ is the body force per unit mass. Surface forces (stresses) are applied directionally on the boundary $\partial\Omega$ and are ascribable to viscous forces. The total vector surface force is derived from the stress tensor $\overleftrightarrow{\sigma}$ (Eq. A.2) as $\mathbf{f}_{\text{surface}} = \nabla \cdot \overleftrightarrow{\sigma}$. The stress tensor is given a more elaborate review in section A.3. In summary, Newton's 2$^{\text{nd}}$ law can be written as

$$\rho\frac{D\mathbf{v}}{Dt} = \rho\mathbf{g} + \nabla \cdot \overleftrightarrow{\sigma}. \tag{2.6}$$

It is insightful to write the stress tensor $\overleftrightarrow{\sigma}$ so that normal stresses σ and shearing stresses τ are labelled explicitly. Effectively, the tensor can be separated into static[VII] and dynamic parts. The first of which comes from the thermodynamic pressure p. The dynamic part, corresponding to off-diagonal components of the stress tensor, is commonly known as the *stress deviator* tensor $\mathbf{T}$. It is responsible for the motion and deformation of the fluid body. In this application the stress tensor is symmetric [7, p. 126] so that $\overleftrightarrow{\sigma}_{ij} = \overleftrightarrow{\sigma}_{ji}$, and angular momentum is conserved.

$$\overleftrightarrow{\sigma}_{ij} = \begin{pmatrix} \sigma_{xx} & \tau_{xy} & \tau_{xz} \\ \tau_{yx} & \sigma_{yy} & \tau_{yz} \\ \tau_{zx} & \tau_{zy} & \sigma_{zz} \end{pmatrix} = -p\mathbf{I} + \begin{pmatrix} \sigma_{xx}+p & \tau_{xy} & \tau_{xz} \\ \tau_{yx} & \sigma_{yy}+p & \tau_{yz} \\ \tau_{zx} & \tau_{zy} & \sigma_{zz}+p \end{pmatrix} = -p\mathbf{I} + \overleftrightarrow{\mathbf{T}} \tag{2.7}$$

[VI] It is common practice to work with intensive variables when possible. To indicate that the equations have been divided by $\Omega(t)$, they are usually denoted with lower-cased letters.

[VII] Of course, there is nothing static about fluid in motion, however the timescale of molecular collisions are sufficiently small so that the fluid is always in local thermodynamic equilibrium [7, p. 16].

2.5 Conservation of Energy

Thermodynamics is a fundamental player in the kinematics of fluid. Heat flow drives fluid motion, just as fluid motion generates heat; the two are reciprocally interrelated. The utility of the conservation of energy becomes readily apparent in problems involving chemical reactions, and the mixing of heterogeneous species.

The equations governing the conservation of energy are resolved using the same techniques put forth in the development of the aforementioned conservation laws. Consider a fluid parcel with volume $\Omega(t)$ enclosed by the surface $\partial\Omega(t)$. The conservation of internal energy per unit mass e and kinetic energy per unit mass $|u|^2/2$ is stated in integral form as:

$$\frac{d}{dt}\int_{\Omega(t)} \rho\left(e+\frac{|\mathbf{u}|^2}{2}\right)\,dV = \int_{\Omega(t)} \rho\mathbf{g}\cdot\mathbf{u}\,dV + \int_{\partial\Omega(t)} \mathbf{f}_{\text{surface}}\cdot\mathbf{u}\,dA - \int_{\partial\Omega(t)} \mathbf{q}\cdot\hat{n}\,dA \quad (2.8)$$

The first two terms on the right are the work done by body forces and surface forces respectively. The last term represents heat transfer through the surface and is associated with the heat flux vector $\mathbf{q}$. As before, this equation is put into differential form by uniting all the terms under one integral for an arbitrary volume. To to this requires a number of tactics: the time differential is brought inside the integral using Reynolds theorem and the surface integrals are converted to volume integrals using the divergence theorem.

Thus far, the conservation of energy equation involves both mechanical and thermal terms. Fortunately, these terms may be separated since it is possible to derive an expression for kinetic energy directly from the conservation of momentum[VIII]. The final result is

$$\frac{De}{Dt} = -p\frac{D(1/\rho)}{Dt} + \frac{1}{\rho}(\tau\cdot\nabla\mathbf{u}) - \frac{1}{\rho}\nabla\cdot\mathbf{q}. \quad (2.9)$$

[VIII] A complete derivation is shown in section 4.8 of Kundu's Fluid Mechanics [7]

In many aspects of chemistry and physics it is more convenient to work with enthalpy h (a measurable quantity) rather than internal energy. The conversion is simple noting that $h = e + p/\rho$. Additionally, Fourier's law of heat conduction states that $\mathbf{q} = -k\nabla T$. Finally, the general form of the energy conservation equation in differential form may be written as

$$\rho \frac{Dh}{Dt} = \frac{Dp}{Dt} + (\tau \cdot \nabla \mathbf{u}) + \nabla \cdot (k\ \nabla T) \tag{2.10}$$

The terms on the right stand for pressure work[IX], viscous work, and heat transfer respectively. The viscous term is a form of irreversible work because the deformed fluid body does not return to its original shape in the absence of viscous stress[7, p. 140]. Note that τ_{ij} is symmetric and can be further simplified with knowledge of the fluids viscosity using the constitutive relation (see section 2.6.1) to write it in terms of the velocity field.

[IX] Actually, the time derivative gives units of power not energy!

Uniting the Conservation Equations

At this point it is clear that the equations governing the general dynamics of fluids (Eq. 2.5, 2.6, 2.10) involve a complicated set of non-linear coupled equations. The system is not yet even closed; we would also need to specify and equation of state. Simultaneously preserving mass, momentum, and energy is task burdensome for even the most powerful computers. Fortuitously, there are scenarios which make the system of equations much more manageable, like for a fluid subject to isothermal conditions. In such an environment energy does not leave the system, and the temperature T can be considered to be constant throughout. A second scenario is the appealing simplification of an incompressible fluid (section 2.6.2). This approximation is justifiable for a large class of liquids and provides informative results even when applied to the gas phase[7, p. 113]. The advantage of studying such a fluid is that the conservation of energy equations become decoupled from the dynamics of the fluid, so that only the equations for the conservation of mass and momentum need to be solved simultaneously.

2.6 Navier-Stokes Equations

In the most general form, the Navier-Stokes equation comes from substituting (Eq. 2.7) into (Eq. 2.6) to give

$$\rho \frac{D\mathbf{u}}{Dt} = \rho \mathbf{g} - \nabla p + \nabla \cdot \overleftrightarrow{\mathbf{T}}. \tag{2.11}$$

On its own, this is equation is not sufficient to solve for the motion of a fluid. To make progress, one would need to know how to determine $\overleftrightarrow{\mathbf{T}}$. Essentially, we need to assume a relationship between the stress and the rate of deformation (strain rate). This is known as a constitutive equation. If we know how the velocity is changing in the direction of the stress we can write $\overleftrightarrow{\mathbf{T}}$ in terms of velocity gradients. This effectively reduces the number of unknowns in the equation; instead of solving for a tensor we are solving for vectors and scalars. Recall that the deviatoric stress is a function of velocity, pressure, and temperature $\overleftrightarrow{\mathbf{T}}(u, p, T)$. One way of modelling $\overleftrightarrow{\mathbf{T}}$ is to assume we are dealing with a Newtonian fluid.

2.6.1 Newtonian Fluid

A Newtonian fluid obeys Newton's law of viscosity ([7, p. 9]). There is a linear relation between the stress σ_{ij} and the strain rate S_{ij} (G.G. Stokes, 1845), which consequently, means that the rank four $(3\times3\times3\times3)$ viscosity tensor μ is independent of velocity. Moreover, a Newtonian fluid is considered to be isotropic, meaning that its intrinsic properties have no preferred direction, or that the stress does not depend on the orientation of the surface [7].

Collectively, these properties, in conjunction with the approximation that the fluid is incompressible $\nabla \cdot u = 0$, leads to some radical simplifications:

- The viscosity tensor reduces to a constant. Note that if the state variables viscosity $\mu(T,p)$ and density $\rho(T,p)$ are constants then the Navier-Stokes equation is decoupled from conservation of energy equations. Effectively, this reduces the number of variables that need to be solved simultaneously. Still, the pressure and velocity must be solved concurrently, however the temperature can be solved independently at another time.

- The constitutive equation relating the stress to the velocity is linear. It is expressed as

$$\overleftrightarrow{\mathbf{T}} = \mu\left(\frac{\partial u_i}{\partial x_j} + \frac{\partial u_j}{\partial x_i}\right) = \mu\left(\nabla\mathbf{u} + (\nabla\mathbf{u})^T\right). \tag{2.12}$$

  Taking the divergence of this, noting that $\nabla\cdot(\nabla\mathbf{u})^T = \nabla(\nabla\cdot\mathbf{u})$ allows the term in parentheses to become.

$$\nabla^2\mathbf{u} + \nabla\cdot(\nabla\mathbf{u})^T \ = \nabla^2\mathbf{u} + \nabla(\nabla\cdot\mathbf{u})$$

  Employing the incompressibility condition $\nabla\cdot\mathbf{u} = 0$ reduces the constitutive equation to

$$\nabla\cdot\overleftrightarrow{\mathbf{T}} = \mu\nabla^2\mathbf{u}. \tag{2.13}$$

2.6.2 Incompressible Navier-Stokes Equations

Working with an incompressible Newtonian fluid has a number of benefits as seen in section 2.6.1. As mentioned previously, this specialization of the Navier-Stokes equation is completely decoupled from the temperature. This means that the conservation of energy equations can be solved independently, reducing the complexity of the problem. Inserting the relation (Eq. 2.13) into (Eq. 2.11) results in the incompressible Navier-Stokes equation

$$\rho \frac{D\mathbf{u}}{Dt} = \rho \mathbf{g} - \nabla p + \mu \nabla^2 \mathbf{u} \tag{2.14}$$

which is a statement of the conservation of momentum. The incompressible form for the continuity equation $\nabla \cdot u = 0$ is a statement of the conservation of mass. Together, these two equations form a system of PDE's with just two unknowns—velocity and pressure.

2.6.3 Physical Interpretation of Navier-Stokes Equations

In deriving the Navier-Stokes equation it was useful to have some physical analogue such as the control volume with which to draw connections. Now that we have the completed equation it is helpful to reinterpret it in a physical sense.

$$\overbrace{\rho\left(\underbrace{\frac{\partial \mathbf{u}}{\partial t}}_{Variation} + \underbrace{\mathbf{u}\cdot\nabla\mathbf{u}}_{Advection}\right)}^{Inertia} = \overbrace{\underbrace{\rho\mathbf{g}}_{ExternalSource}}^{Body} - \overbrace{\underbrace{\nabla p}_{InternalWork} + \underbrace{\mu\nabla^2\mathbf{u}}_{Diffusion}}^{Surface} \tag{2.15}$$

The terms on the LHS (see Section A.2: Material Derivative) represent the motion of the fluid due to the combined effect of the external, hydrostatic, and viscous forces that are summarized on the RHS. External sources such as gravity act on the entire body, whereas internal forces such as those associated with $-\nabla p$ and $\mu\nabla^2 v$ act on the surface[X]. The $-\nabla p$ term prevents the volume from compressing due to normal stresses; instead it deforms and moves the fluid body. The advection and diffusion terms are defined below:

[X] Keep in mind that the surface referred to here is part of an artificial volume inside the fluid.

- **Advection**: the movement of a fluid parcel due to the velocity field. One way of thinking about this might be to realize that the dot product in $\mathbf{u} \cdot \nabla \mathbf{u}$ is projected along the velocity vector, and is largest when the velocity is changing in the direction of the flow ($\nabla \mathbf{u} \parallel \mathbf{u}$). In other words, local areas of flow tend to align towards the bulk stream.
- **Diffusion**: The diffusivity term $\mu \nabla^2 \mathbf{u}$ takes advantage of resistive forces (inflicted by the shearing stresses between viscous fluid layers) to propagate momentum; basically, fluid in motion will drag surrounding fluid with it. The Greek letter μ stands for the dynamic viscosity with units of (Force·Time/Area). It is common to divide through by ρ, where ratio μ/ρ is defined as the *kinematic viscosity* and is often referred to as "momentum diffusivity". A high viscosity fluid is not as miscible as a low viscosity one.

2.7 Boundary Conditions

Formulating a mathematical problem such as the Navier-Stokes equations requires, in addition to the governing equations, two things: a detailed depiction of the geometry (the domain in space where the equations are being solved), and boundary conditions.

Boundary conditions provide indispensable information concerning the unknowns in the equation. The two main types of boundary conditions are the Dirichlet and Neumann conditions:

- **Dirichlet**: Specifies the value of the function on a surface, $\mathbf{u}(\mathbf{x}, t) = f(\mathbf{x}, t)$ on $\Gamma_D \subset \partial\Omega$.
- **Neumann**: Specifies the normal derivative of the function on a surface, $\frac{\partial \mathbf{u}}{\partial n} = \nabla \mathbf{u} \cdot \hat{n} = f(\mathbf{x}, t)$ on $\Gamma_N \subset \partial\Omega$. It is common to set $f(\mathbf{x}, t) = 0$, in which case it is referred to as a natural or "do nothing" boundary condition; it say that the velocity will not change beyond that point in the direction of the normal.

Typically, for viscous flows, a Dirichlet noslip condition of of $\mathbf{u} = 0$ is employed everywhere on the boundary. This ensures that the fluids velocity is zero at the solid interface, and is justifiable when fluid-fluid cohesive forces are surpassed by fluid-solid forces.

In this thesis, we consider closed boundary everywhere except an inlet and outlet for the geometry. One way of driving the flow is to setup a pressure gradient using Dirichlet pressure conditions of unique value at the inlet and outlet of the geometry. Alternatively, an unchanging velocity profile can be defined using a Dirichlet velocity condition at the inlet and a Neumann "do nothing" boundary condition at the outlet. This second method will not work in the absence of a pressure condition; it is mandatory to specify the pressure somewhere within the domain!

In addition to boundary conditions it is also necessary to supply initial conditions. In this thesis, the goal is to find a steady state solution to the fluid flow. The approach used here is to start with an initial condition of zero velocity everywhere and let the system spin up to equilibrium as the initial transients decay. Although, an educated guess at the solution could speed up its convergence[XI].

2.7.1 The Boundary $\partial\Omega$

The boundary can be defined as the union of the boundaries associated with the three types of boundary conditions: the Dirichlet, Neumann, and Robin Condition. The latter will not be considered in this thesis.

$$\partial\Omega = \Gamma_D \cup \Gamma_N \cup \Gamma_R \tag{2.16}$$

[XI] Some experimentation was done with various boundary and initial conditions and it was discovered that some of them brought the system to steady state faster than others (See Section 4.2).

Chapter 3

Discretization of PDE's

The majority of PDEs in fluid dynamics are unsolvable by current analytical methods. Instead, approximate solutions must be derived numerically. Although a variety of numerical schemes exist, the approach taken in this thesis begins with writing the differential equation in weak form (Section: 3.1). In short, this involves multiplying a PDE by a so-called *test* function then integrating over the entire fluid domain. The advantage of integrating is that it makes it easier to specify boundary conditions (Section: 2.7) over complex geometries.

The next step is the temporal discretization. As with many time-dependent numerical problems, the equations must be written in an iterative form, progressing with some time step. This can be achieved using finite difference methods for numerical differentiation. Here, we use a predictor-corrector numerical schemes that is appropriate to solve the Navier-Stokes equations. This scheme, called the Incremental Pressure Correction Scheme, is described in Section 3.3.1.

The final step involves spatially discretizing the domain into elements with a process called *meshing* (Section: 3.4.1). The PDE is solved in each substituent element making up the domain and a total field is interpolated by uniting each of these solutions. This idea is known as the *Finite Element* method (Section: 3.2).

3.1 Variational Formulation

The first step in solving a PDE is to reformulate it as a *variational* problem. The term stems from calculus of variations: the field of mathematics concerned with minimizing or maximizing a functional. One can cast the problem into a weak form by multiplying the PDE by a special test function v and integrating over the domain Ω. It is the presence of the test function that weakens the requirement for the solution u to be defined at all points, so that discontinuous derivatives are allowable. In general, it is much easier to solve a differential (strong) equation in its integral (weak) form. It also makes the task of enforcing boundary conditions much more natural, as they are now carried out over an integral relatable to the geometry. While the weak form is clearly different from the differential equation, it can be shown that a solution to the weak equation is also a solution to the strong equation. Variational methods lay the groundwork for FEA.

3.2 Finite Element Method

The variational form of a PDE is a continuous problem with an infinite number of unknowns[I]. We can approximate the solution of some field $u(x)$ by solving a similar discrete problem with a finite number of unknowns. We introduce the approximate solution $u_h(x)$ which differs from the true solution by some error $u(x) = u_h(x) + e(x)$.

The idea of Finite Element Analysis is to describe a general function using simple functions, called the basis. This technique subdivides the problem into smaller elements which are easier to work with. The advantage of this is that the equation is now separable. In practice, PDEs are solved over individual elements, then accumulated to form the complete solution.

[I]The unknowns are the undetermined coefficients of (Eq. 3.1), U_j. In the limit as j goes to infinity, the approximation $u_h(x)$ approaches the true solution $u(x)$.

The function $u_h(x)$ can be expanded in terms of the basis ϕ_j, which is part of the N-dimensional trial space[II] V_h, as

$$u_h(x) = \sum_{j=1}^{N} U_j \phi_j(x). \tag{3.1}$$

In essence, U_j is the weight of a particular function used to manufacture $u_h(x)$. In Finite Element Analysis, the basis is chosen but their respective weights are to be determined. As an example, consider Figure 3.1, where the wave $\Psi = \alpha\phi_1 + \beta\phi_2$ is decomposed into two sinusoidal basis functions ϕ each weighed by some undetermined coefficient α and β.

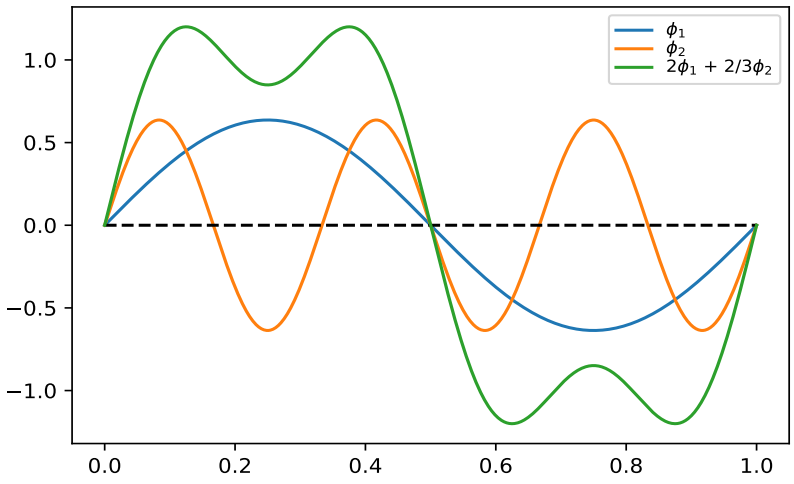

Figure 3.1: An example of sinusodial basis functions that are being superimposed to create the function Ψ (colored green).

In keeping with the variational methods it is necessary to redefine the test function ν in terms of basis functions as well. Indeed, this basis does not have to be the same as for $u_h(x)$. To avoid loss in generality a separate function space, the test space $\hat{V}_h$, is defined. Within this space is a class of functions $\{\hat{\phi}_i\}$ which form the basis. That is,

$$v_i = \hat{\phi}_i(x). \tag{3.2}$$

[II]Function space is discussed more rigorously in Section 3.2.1. Until then, it suffices to think of it as a restrictive environment housing very particular functions.

With a convenient basis at hand, the next step is to substitute (Eq. 3.1) and (Eq. 3.2) into the variational formulation. The great deal with this is that it turns the system of PDEs into a simple algebraic problem, $Au = b$. To exemplify this consider the following exercise.

A Simple Example: Poisson's Equation

Suppose we wish to solve the familiar Poisson's equation (elliptic) for u, where f and u_D are known functions on the domain Ω or its boundary $\partial\Omega$.

$$\begin{aligned} -\nabla^2 u(\boldsymbol{x}) &= f(\boldsymbol{x}), \quad \boldsymbol{x} \text{ in } \Omega, \\ u(\boldsymbol{x}) &= u_{\text{D}}(\boldsymbol{x}), \quad \boldsymbol{x} \text{ on } \partial\Omega. \end{aligned}$$

The variational form is actualized using integration by parts, acknowledging that the test function v is zero on the surface due to the Dirichlet condition [11]:

$$\int_\Omega f v \; dx = \int_\Omega \nabla u \cdot \nabla v \; dx \qquad\qquad \forall \; v \in \hat{V}$$

Substituting equations 3.1 & 3.2 into this yields a system of linear equations ($A_{ij}U_j = b_i$)

$$\sum_{j=1}^{N} U_j \int_\Omega \nabla \phi_j \cdot \nabla \hat{\phi}_i \; dx = \int_\Omega f \hat{\phi}_i \; dx,$$

Which can be inverted to solve for the coefficient matrix U. Notice that

$$A_{ij} = \int_\Omega \nabla \phi_j \cdot \nabla \hat{\phi}_i \; dx \qquad , \qquad b_i = \int_\Omega f \hat{\phi}_i \; dx.$$

3.2.1 Basis Functions & Vector Space

Function Space

We have made use of the *trial* and *test* function spaces but they have not yet been properly defined. A function space is an abstract vector space. The important thing about them, in the context of fluid dynamics, is that they constrain the solution to functions of a particular form. One example used in a number of physics applications is the Lagrange $\mathbb{L}^2$ function space, which requires functions to be square integrable so that $\langle f|f\rangle$ is finite. Despite being an infinite dimensional space, it retains a geometrical significance comparable to the Euclidean frame $\mathbb{R}^3$, and is therefore a Hilbert space.

Basis Functions

The choice of basis is pivotal when it comes to accurately representing a function. Ordinarily, the basis is restricted to a particular class of functions whose properties are sought after. This limitation is naturally ensued by the selection of a specific function space. A highly versatile option is the polynomial basis of the Lagrange $\mathbb{L}^2$ function space, which is usually restricted to a particular order (linear, quadratic, etc.). The degree elected is paramount when it comes to the success of the fit[III]. Figure 3.2 illustrates both linear and quadratic $\mathbb{L}^2$ basis elements. One can imagine that any continuous function can broken into a series of infinitesimally small line segments (linear basis elements). However, since we are dealing with a finite number of nodes (points along x) we may need to increase the order of the basis to fit the function.

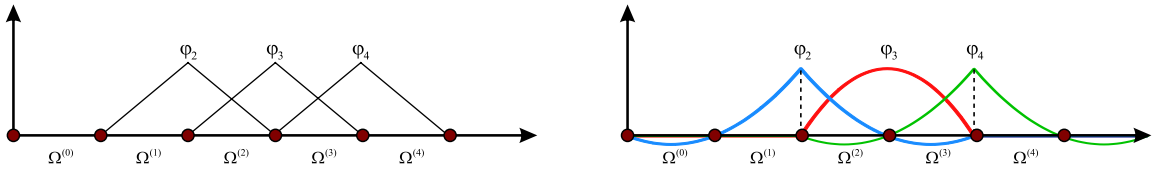

(a) Linear Basis **(b)** Quadratic Basis

Figure 3.2: $\mathbb{L}^2$ Basis Functions.

[III] Selecting the wrong basis could lead to oscillations that prevent the functions from ever converging [10, p. 62].

In problems involving multiple variables, it is standard to define a unique function space for each unknown; the basis representing one function may not be good at representing another, therefore two independent sets of basis are used. In fact, when solving Navier-Stokes equations it is common to search for velocity solutions of quadratic form (Figure 3.2b), whereas the pressure solution is sufficiently detailed using linear functions[11] (Figure 3.2a).

3.3 Variational Form of Navier-Stokes

Consider the incompressible Navier-Stokes equations below. For steady[IV] viscous flows this PDE is smooth with a continuous derivative. For convenience, the terms containing the unknowns, $\mathbf{u}$ and p, have been written on the LHS, as in

$$\rho\frac{\partial \mathbf{u}}{\partial t} + \rho(\mathbf{u}\cdot\nabla\mathbf{u}) - \mu\nabla^2\mathbf{u} + \nabla p = \mathbf{f} \tag{3.3a}$$

$$\nabla\cdot\mathbf{u} = 0. \tag{3.3b}$$

To write this in its weak form multiply (Eq. 3.3a) by a test function ν, and integrate over the domain Ω, giving

$$\int_\Omega \rho\frac{\partial \mathbf{u}}{\partial t}\cdot\nu\ dx + \int_\Omega \rho(\mathbf{u}\cdot\nabla\mathbf{u})\cdot\nu\ dx - \int_\Omega \mu\nabla^2\mathbf{u}\cdot\nu\ dx + \int_\Omega \nabla p\cdot\nu = \int_\Omega \mathbf{f}\cdot\nu\ dx. \tag{3.4}$$

A standard approach in breaking equations like these down is to lower the order of the derivatives. This is done using integration by parts,

$$\int f\left(\frac{dg}{dx}\right)dx = \int \frac{d}{dx}(fg)dx - \int g\left(\frac{df}{dx}\right)dx.$$

The diffusive term can then be expressed as

$$-\int_\Omega \mu\left(\nabla^2\mathbf{u}\right)\cdot\nu\ dx = -\int_{\partial\Omega}\mu\frac{\partial\mathbf{u}}{\partial n}\cdot\nu\ ds + \int_\Omega \mu(\nabla\mathbf{u}\cdot\nabla\nu)\ dx.$$

[IV] Surprisingly, it is easier to solve for unsteady viscous flows as the PDE is parabolic rather than elliptic. In practice, a steady flow can be converted to unsteady using a time-marching scheme [3].

The surface integral comes from the realization that the limits of integration lie on the boundary of the volume, and the sign correlates with the direction of the surface normal. The pressure gradient term is found to be

$$\int_\Omega (\nabla p \cdot \nu)\ dx = \int_{\partial\Omega} p\nu \cdot \hat{n}\ ds - \int_\Omega p\nabla \cdot \nu\ dx.$$

The resulting equation, as well as the one preceding it, can be further simplified using the fact that the test function v is required to vanish on the (Dirichlet) boundary Γ_D [11], where the solution is known, leaving only only the portion of the surface with Neumann boundary conditions, Γ_N. Equivalently, $\partial\Omega = \Gamma_D \cup \Gamma_N \to \Gamma_N$ so that

$$\int_\Omega \rho\frac{\partial \mathbf{u}}{\partial t} \cdot \nu\ dx + \int_\Omega \rho(\mathbf{u} \cdot \nabla \mathbf{u}) \cdot \nu\ dx + \int_\Omega \mu(\nabla \mathbf{u} \cdot \nabla \nu)\ dx$$
$$- \int_\Omega p\nabla \cdot \nu\ dx + \int_{\Gamma_N} p\nu \cdot \hat{n}\ ds - \int_{\Gamma_N} \mu\frac{\partial \mathbf{u}}{\partial n} \cdot \nu\ ds = \int_\Omega \mathbf{f} \cdot \nu\ dx.$$

Similarly, the incompressiblity condition gets put into a weak form using its own test function q, and integrating over Ω as in $\int_\Omega \mathbf{q}\ \nabla \cdot \mathbf{u} = 0$. Compiling everything so far completes the variational formulation, which is presented as

$$\int_\Omega \{\rho\frac{\partial \mathbf{u}}{\partial t} \cdot \nu + \rho(\mathbf{u} \cdot \nabla \mathbf{u}) \cdot \nu + \mu(\nabla \mathbf{u} \cdot \nabla \nu) - p\nabla \cdot \nu\}\ dx$$
$$= \int_\Omega \mathbf{f} \cdot \nu\ dx + \int_{\Gamma_N} \{\mu\frac{\partial \mathbf{u}}{\partial n} \cdot \nu - p\nu \cdot \hat{n}\}\ ds, \qquad \forall \nu \in \hat{V}^{\text{V}} \qquad (3.5a)$$

$$\int_\Omega \mathbf{q}\ \nabla \cdot \mathbf{u} = 0, \qquad \forall \mathbf{q} \in \hat{Q} \qquad (3.5b)$$

[V] This says the test function ν belongs to the function space $\hat{V}$. The idea of a function space will be introduced in Section 3.2.1

3.3.1 Chorins Method & IPCS

The idea of temporal discretization is to cast the problem into an iterative form which can be implemented in a computer program. When translating a differential equation to a computer it is customary to approximate the derivatives with finite differences. In this work, it suffices to use simple difference quotients to approximate time derivatives. For example, a first order derivative may be approximated using one of the following methods:

$$\left(\frac{\partial u}{\partial t}\right)_i \approx \frac{u_{i+1} - u_i}{\Delta t} \qquad \text{Forward Difference} \tag{3.6}$$

$$\left(\frac{\partial u}{\partial t}\right)_i \approx \frac{u_i - u_{i-1}}{\Delta t} \qquad \text{Backward Difference} \tag{3.7}$$

$$\left(\frac{\partial u}{\partial t}\right)_i \approx \frac{u_{i+1} - u_{i-1}}{2\Delta t} \qquad \text{Central Difference.} \tag{3.8}$$

In application to the NS equations, these methods result in a nonlinear problem which is not very straightforward to solve. The task is especially cumbersome due to the fact that the velocity and the pressure are coupled by the incompressibility constraint (Eq. 3.3b). A more efficient approach was brought forth by Chorin (1968) as the so called projection method. One of the many variations of the scheme is known as the Incremental Pressure Correction Scheme (IPCS) [4]. As the name suggests, it is an iterative algorithm. The majority of its success comes from the fact that it decouples the velocity and pressure and solves them independently as a set of elliptic equations ([5]). It is therefore classified as a *splitting* method. The routine involves calculating a *tentative*[VI] velocity $u^\star$ using an estimate for the pressure (obtained from the previous time step if there is one), using this velocity to obtain a better representation of the pressure, and finally using the adjusted pressure to compute the corrected velocity. As a result, the variational formulation assumes three steps as presented below, where the time derivative is approximated using a central difference scheme.

[VI] A tentative velocity is a temporary guess at the solution based on the given pressure. Its purpose is to essentially find agreement between the pressure and velocity.

IPCS Scheme

The Incremental Pressure Correction Scheme is not derived or explained in detail in this thesis. For more information see the originating article by Goda [4] and Section 3.4 of the FEniCS tutorial [10, p. 56-73]. The scheme is presented as follows:

$$\langle \frac{\rho}{\Delta t}(u^\star - u^n), v\rangle + \langle \rho u^n \cdot \nabla u^n, v\rangle + \langle \sigma(u^{n+\frac{1}{2}}, p^n), \epsilon(v)\rangle + \langle p^n n, v\rangle_{\partial\Omega} - \langle \mu \nabla u^{n+\frac{1}{2}} \cdot n, v\rangle_{\partial\Omega} = \langle f^{n+1}, v\rangle. \tag{3.9}$$

$$\langle \nabla p^{n+1}, \nabla q\rangle = \langle \nabla p^n, \nabla q\rangle - \frac{1}{\Delta t}\langle \nabla \cdot u^\star, q\rangle. \tag{3.10}$$

$$\langle u^{n+1}, v\rangle = \langle u^\star, v\rangle - \frac{1}{\Delta t}\langle \nabla(p^{n+1} - p^n), v\rangle. \tag{3.11}$$

Where $\epsilon(u) = \frac{1}{2}\overleftrightarrow{\mathbf{T}}$ and $\sigma(u,p) = 2\mu\epsilon(u) - pI$ as seen in Chapter 2, v and q are well chosen test functions and all of the remaining variables are as previously defined. The notation $u^{n+\frac{1}{2}}$ refers to the arithmetic mean $u^{n+\frac{1}{2}} \approx \frac{(u^n + u^{n+1})}{2}$ and $\langle v, w\rangle = \int_\Omega vw\ dx$. Implementation of the IPCS into the finite element software FEniCS may be found in [12, p. 402]

3.4 Spatial Discretization: Mesh

It can be enormously difficult to solve a PDE over a complex geometry. The standard approach is to discretize the domain into elements of primitive geometry such as triangles or tetrahedrons. Collectively, these elements form the mesh, which is an approximate depiction of the geometry. A single element of the mesh is called a cell. Figure 3.3 shows Lagrangian elements of order 1, denoted by $P1$.

Increasing the order of the element increases the number of nodes within the cell. These nodes, indicated by the black dots, serve as evaluation points. Referring back to Figure 3.2, a greater number of nodes corresponds to a better fit of the solution using appropriate basis functions. Figure 3.4 shows Lagrangian elements of order 2, denoted by $P2$.

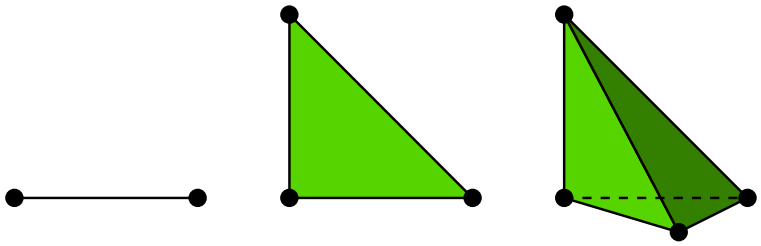

Figure 3.3: $P1$ Lagrange elements in 1-3 dimensions. There is a node at every vertex. Taken with permission from the FEniCS book [12].

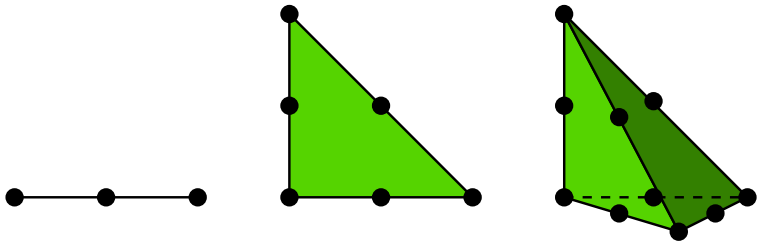

Figure 3.4: $P2$ Lagrange elements in 1-3 dimensions. There is a node at every vertex and one at middle of each edge. Taken with permission from [12].

In addition to systemically detailing the geometry, the mesh retains information regarding boundary conditions. Selected cells, or rather their facets, might be assigned Dirichlet or Neumann conditions, in which case they are referred to as the Γ_D and Γ_N parts of the boundary $\partial\Omega$ (Section 2.7.1).

The usefulness of the mesh elements is that they provide a simple geometry for solving PDEs. Keep in mind the objective of discretization is to divide a complicated problem into many simple ones, which can later be assembled to approximate the complete solution. Each individual cell in the mesh accommodates a fairly simple function which must satisfy the governing equations with appreciation for the other cells in its local environment. Recall that the form of these functions depends on the type and order of the element (Figures 3.3 and 3.4). Consequently, the accuracy of the solution depends on the size of the cells; to resolve finer detail demands smaller cells, or more evaluation points. Dividing the mesh into smaller elements dramatically increases the complexity of the problem, and therefore the computational time required to solve it.

3.4.1 Meshing

In general a mesh is built by first defining a geometry, then dividing it into many small elements using some triangulation technique. Typically, the geometry is outlined by either parameterizing a surface enclosing the volume, or constructively adding together simple shapes such as rectangular prisms and cylinders. The latter approach is known as Constructive Solid Geometry (CSG). There are several existing software programs, both commercial and open source, that can be used for meshing. The program used in this thesis is called *mshr*: a tetrahedral mesh generator that uses CSG and supports a number of meshing algorithms. This will be explored in Section 4.1.

CFD is known for its struggle with large data sets and long computation time. Although the first instinct might be to provide compensation with more powerful computers, there are more effective approaches. One improvement is to optimize the size of the mesh cells. It is known that smaller cells yield more accurate results, but create a much more computationally demanding problem. Therefore, it is wise to look for a balance between cell size and time requirements. Even better would be to increase mesh resolution only where it is needed. This method is called local mesh refinement. An example of a locally refined mesh is shown in Figure 3.5.

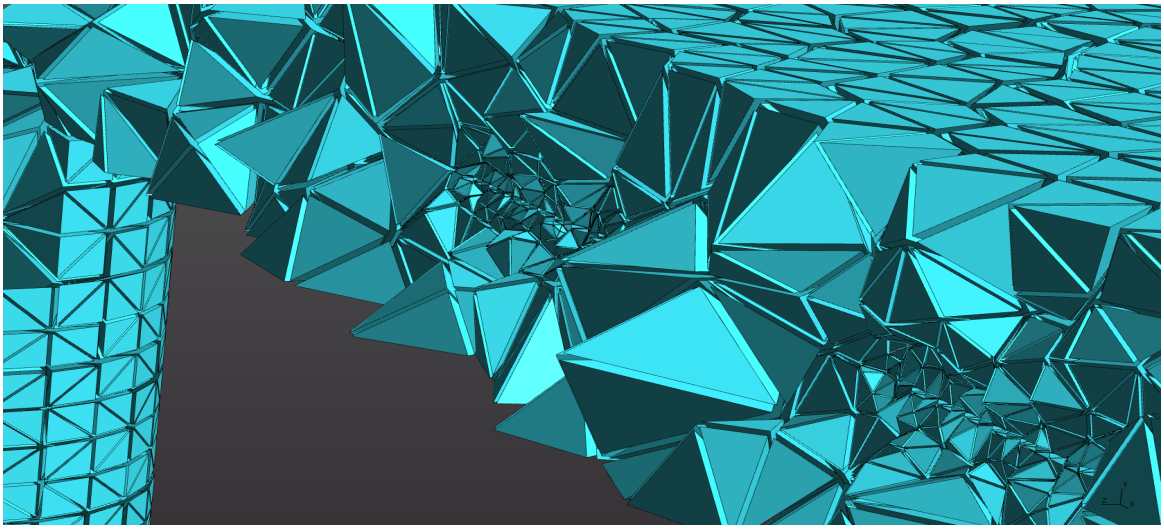

Figure 3.5: Artistic representation of a tetrahedral mesh. Part of the mesh has been removed to show the inside. Notice how the elements vary in size; this mesh has been refined locally to optimize the quality of the solution only where it is needed.

Chapter 4

Cantilever Specific Problem

In this chapter, we make use of the methods and ideas developed in previous sections to study fluid flow through the cantilever cell. The problem introduced in Chapter 1 is established mathematically in rigorous detail. We begin by specifying the domain of the fluid, which is used to manufacture a mesh. Then proceed by concisely stating all the equations and boundary conditions that are involved. The results of the CFD simulation are presented in this chapter, along with some experiments that justify whether or not the solution appears to be valid. One of the most significant studies used in the development of the program is of the flow development at the inlet. In this region the geometry is very simple and can be compared with the analytical solution for pipeflow; if the numerical solution is in agreement with the analytical result, then there is some assurance that the problem has been defined correctly. The results of the CFD analysis in the long-time limit are carefully examined with a clear focus on the flow around the cantilevers.

4.1 Domain of Interest

A tetrahedral mesh was created using CSG with primitive shapes such as rectangular prisms and cylinders to replicate the domain seen in Figure 4.1, using the exact measurements exhibited in Listing 4.1. This was accomplished with the open source software, *mshr*[I], which was interfaced using code written in *Python*. The Python interface is preferred over a graphical one because it is more reproducible and can be easily modified.

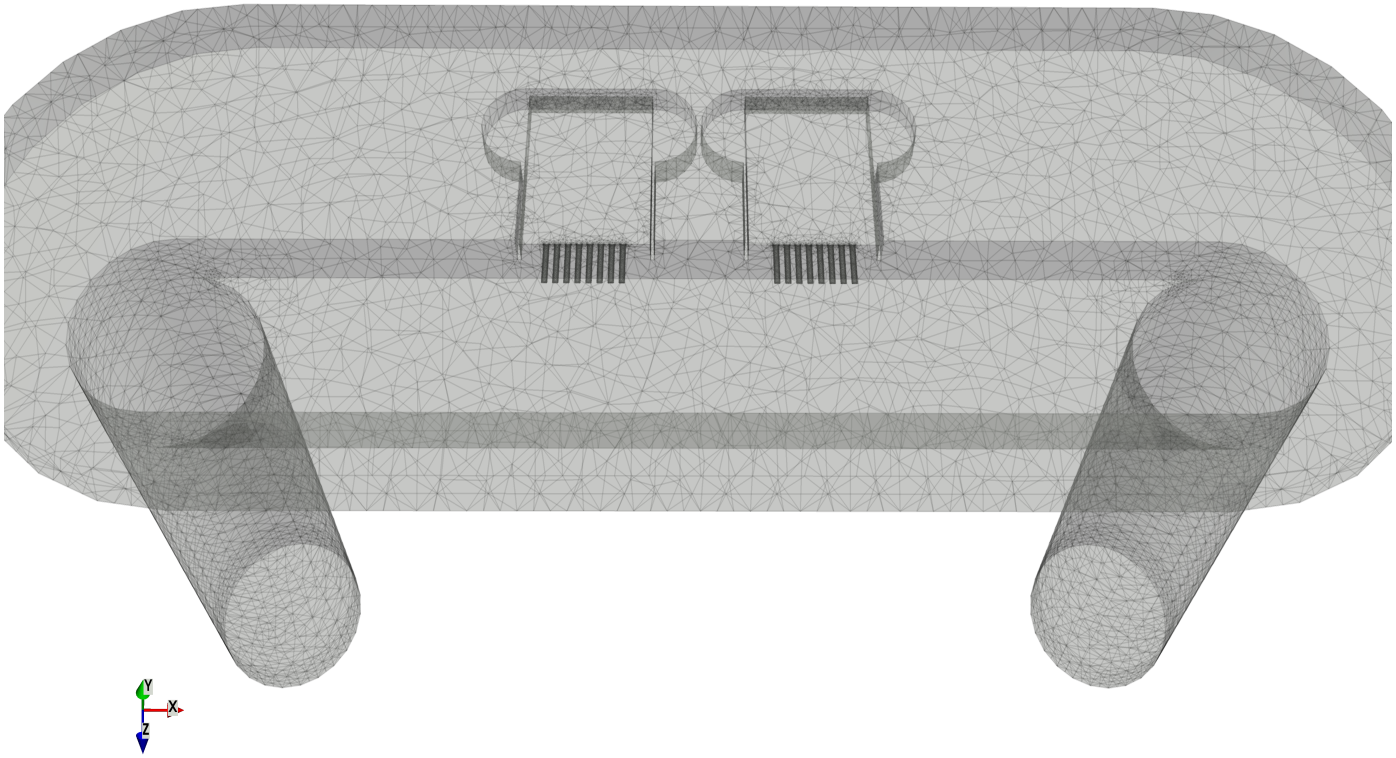

Figure 4.1: The fluid domain. It represents everywhere that fluid exists in the cantilever cell, and is the environment where simulation is done—the mesh. Although the cantilevers, and the block to which they are attached appear to be part of the domain, they are actually excluded from the fluid volume. The only reason these features are apparently visible is because of the shading used on the interior surface to make it that way. The origin is placed at the center of the inlet orifice: X is directed to the right, Y along the axis of the pipe, and Z, with righthandedness, in the plane of the top surface. Edges cropped to fit page.

[I] https://bitbucket.org/fenics-project/mshr/src/master/

Listing 4.1: Domain Measurements

```
"#========================System Dimensions (Millimeters)========================#"
#Cell Block to which the Cantilevers Attach.
f(0)  = Block_Length           = 3.1    mm     # Cell Block Length
f(1)  = Block_Thickness        = 0.4    mm     # Cell Block Thickness
f(2)  = Block_Width            = 2.4    mm     # Cell Block Width

#Cantilever Dimensions
f(3)  = Cantilever_Length      = 0.75   mm     # Cantilever Length (750 ± 3 μm)
f(4)  = Cantilever_Separation  = 0.1    mm     # Space between Cantilevers
f(5)  = Cantilever_Thickness   = 0.001  mm     # Cantilever Thickness (1 ± 0.1 μm)
f(6)  = Cantilever_Width       = 0.1    mm     # Cantilever_Width

#Indentation (Section under the glass plate)
f(7)  = Groove_Depth_y         = 1.016  mm     # Groove[II] Depth
f(8)  = Groove_Length_x        = 19.05  mm     # Groove Length Center to Center Hole
f(9)  = Groove_Offset_X        = 0.767  mm     # Groove Offset
f(10) = Groove_Offset_Z        = 1.235  mm     # Groove Offset
f(19) = Window_Depth_y         = 1.0    mm     # Window Depth (Estimated 1mm)
f(20) = Window_Width_z         = 8.89   mm     # Window Width

#Cantilever Holder
f(11) = Holder_CircleDiameter  = 1.588  mm     # Circular Extrusion behind Cell Block
f(12) = Holder_Depth_y         = 0.508  mm     # Cantilever Holder Depth
f(13) = Holder_Length_z        = 3.175  mm     # Cantilever Holder Length
f(14) = Holder_Separation_x    = 1.667  mm     # Cantilever Holder Width
f(15) = Holder_Width_x         = 2.54   mm     # Holder Separation

#Pipe
f(16) = Pipe_Length_Left_y     = 9.296  mm     # Length of Left Pipe (Axis along y)
f(17) = Pipe_Length_Right_y    = 9.296  mm     # Length of Right Pipe
f(18) = Pipe_Radius            = 1.588  mm     # Radius of Inlet/Outlet Pipe
```

Table 4.1: Mesh Specification

Property	Value
Volume	0.436 ml
Surface Area	750.4 mm^2
Number of Cells	373907
Number of Vertices	73541

[II] Groove is small channel where cantilevers are situated

The mesh generator *mshr* supports a number of different triangulation algorithms, including *CGAL*[III] and *Tetgen*[15]. Due to the complexity of the geometry, and the tiny scale of the microcantilevers in comparison with the rest of the domain, many of the meshing algorithms failed to draw any tessellations[IV]. Figure 4.2a illustrates an attempted meshing of a single cantilever (0.001 mm thick) mounted to the cell block (0.4 mm thick). Clearly, CGAL is having problems around sharp edges and small features. Although the holes in the mesh appear most strikingly, the regions of dense nodes (dark areas) are equally problematic. These issues come from trying to create a flat surface using tetrahedrons. This is where another software, Tetgen succeeds over its competitors—it preserves the surface of the mesh and can adapt to extreme size differences by varying the size of its cells (Figure 4.2b). Notice that the number of grid points is much more dense on the cantilever then anywhere else. This is desirable as the cantilevers are the interest of this experiment, so the more data points the better. The mesh used in this work (Figure 4.1) is characterized in Table 4.1.

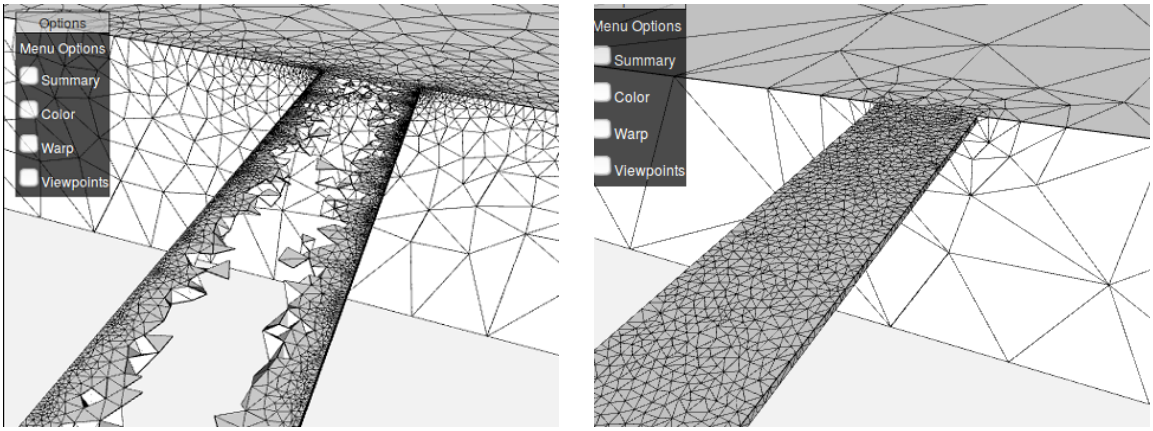

(a) CGAL **(b)** Tetgen

Figure 4.2: Triangulation Algorithms: CGAL vs. Tetgen.

[III] https://www.cgal.org/index.html

[IV] A tessellation defines how points connect together. In this mesh they form tetrahedrals that fit together perfectly so that there are no holes in the interior.

4.2 Restatement of the Problem

The goal of this problem is to solve for the velocity and pressure fields in the system using the Navier-Stokes equation for incompressible flows (Eq. 2.14). When implementing this as a computer program it is actually preferable to use a slightly more rudimentary form that externalizes the incompressibility condition. This is to avoid the second order derivatives that arise when trying to simplify equation 2.12. The final form of the incompressible Navier-Stokes equation is summarized by the following equation:

$$\rho\left(\partial\mathbf{u}/\partial t + \mathbf{u}\cdot\nabla\mathbf{u}\right) = \nabla\cdot\sigma(\mathbf{u},p) + \mathbf{f} \tag{4.1a}$$

$$\sigma(\mathbf{u},p) = \mu\left[\nabla\mathbf{u} + (\nabla\mathbf{u})^T\right] - pI \tag{4.1b}$$

$$\nabla\cdot\mathbf{u} = 0, \tag{4.1c}$$

where $\sigma(\mathbf{u},p)$ is the stress tensor, and $\mathbf{f}$ is the body force. The remaining characters follow standard symbolism (see prefatory for Nomenclature). In this model, it is logical to presume that body forces such as gravity will have very little impact on the overall fluid motion. Therefore, $\mathbf{f}$ is set to zero.

Boundary Conditions

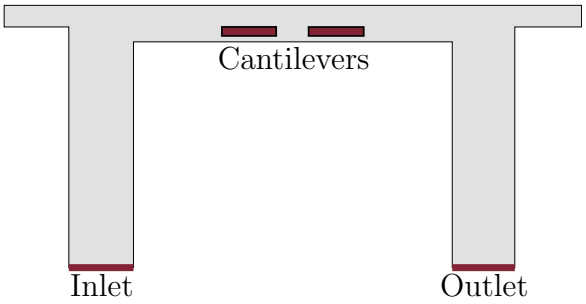

Figure 4.3: A simple sketch of the complete 3D fluid domain highlighting boundary parts.

Figure 4.3 shows a simple schematic representation of the fluid domain. The different parts of the boundary are identified as: the inlet, outlet, and the cantilevers. The remainder of the surface is referred to as the walls. Recall from section 2.7.1 that the boundary may be defined mathematically using a combination of Dirichlet and Neumann conditions. Those that are essential in solving this problem are discussed below.

- **Walls**:

  The walls of the domain are rigid and impenetrable. To ensure that no fluid passes through these walls the velocity normal to the surface is required to vanish in this region. Supposing that the fluid-solid adhesive forces are stronger than fluid-fluid cohesive forces near the boundary, then the tangential velocity will be small enough that it can be reasonably approximated as zero as well. This is known as the "no-slip" condition:

  $$\Gamma_{wall}: \quad \vec{u} = 0$$

  It reads: "for the wall part of the boundary (denoted by Γ_{wall}) the velocity (normal and tangential) is zero".

- **Cantilevers**:

  In the current study the cantilevers are rigid. They adopt the same no-slip condition as the walls and, therefore, act only as an obstruction to the flow in the cell.

  $$\Gamma_{cantilevers}: \quad \vec{u} = 0$$

- **Outlet**:

  At the outlet, fluid must be able to leave the system. This can be accomplished with a Neumann condition, $\nabla\vec{u} \cdot \hat{n} = 0$, which says that the normal component of the velocity is constant beyond the outlet. Effectively, once the fluid leaves the outlet it moves freely out of the way, having nothing more to do with the system.

  In addition to the condition of the velocity, there must also be one for pressure. It is necessary to set the pressure somewhere in the system. The choice of pressure is arbitrary since it is really a pressure difference that drives the flow. For convenience the pressure at the outlet is set to zero.

  $$\Gamma_{Oulet}: \quad \nabla\vec{u} \cdot \hat{n} = 0, \quad P = 0$$

- **Inlet**:

  The flow can be driven in one of two ways:

  I. A pressure gradient is set up that will accelerate the fluid in the direction of low pressure. This effect is easily administrated using conditions similar to the outlet, except for a nonzero constant pressure P_0 at the inlet:

  $$\Gamma_{Inlet}: \quad \nabla\vec{u}\cdot\hat{n}=0, \quad P=P_0.$$

  II. A velocity profile is prescribed at the inlet that forces fluid through the cell by transferring its momentum:

  $$\Gamma_{Inlet}: \quad \vec{u}=f(\vec{\mathbf{x}},t).$$

  Since the form of the inlet velocity profile is not known, the first method (I) is used. This method is especially good for analyzing developing flows in a time-dependent manner, and is able to establish a flow profile without any wrongful conjectures to its form. Unfortunately, however, it might not be the most efficient choice when it comes to computer modelling. Following the discussion of Chapter 3: the velocity was chosen to be represented with a $\mathbb{L}^2$ quadratic basis using $P2$ Lagrange elements, whereas the pressure is represented using a linear basis and $P1$ elements. Presumably, a boundary condition on the velocity will be much stronger than the pressure simply because there are more evaluation points. In this study the IPCS was found to be much more stable when prescribing the inlet velocity rather than an inlet pressure! The solution reached convergence much faster using this method, saving a lot of simulation time.

In this study both methods are explored, however the latter is only used in place of steady state profiles where $\vec{u}=f(\vec{\mathbf{x}},t)\rightarrow f(\vec{\mathbf{x}})$. The general procedure is as follows. Using an inlet boundary condition in the form of (I) generate a solution for the velocity in the long-time limit. Using numerical surface fitting techniques find an approximate expression u_e for the inlet velocity profile. Finally, redefine the problem using method (II) now with u_e enforced as a Dirichlet condition. This routine helped save many days worth of simulation time for the work presented in this thesis.

Initial Conditions

Initially the velocity is zero everywhere within the system: $\vec{u}(\vec{\mathbf{x}}, t_0) = 0$. Although these initial conditions are sufficient for FEA they do not match with the boundary conditions; initially the velocity is zero everywhere within the domain, however at the very first time step the velocity on the boundary of the inlet is largely nonzero. For the velocity at the orifice to drastically change from zero to a large number in a infinitesimal amount of time there must be a very large force (acceleration). Physically, this discontinuity sends a pressure shock wave through the volume. Fortunately, the iterative correction scheme quickly loses track of the initial conditions so this problem is not catastrophic in long time limits.

4.2.1 Validity of Numerical Solution

When it comes to simulating fluid, the success of the solver is heavily reliant on the quality of the mesh—the credibility of the numerical approximation increases with the resolution of the mesh. Of course, such detailed approximations come at a cost of computing time. Somewhere in the balance between quality and time there exists a mesh that is fine enough to yield reasonable results, but not so fine that it consumes unnecessary computing resources. In other words, the error attributed to the numerical approximation should decay as the solver progresses, or it should converge to a particular result. Whether or not the result is correct requires further interpretation, which may be accomplished in a number of ways, such as: through direct comparison with the analytical solution, or by studying the convergence of the solution.

Since a problem such as this does not have an analytical solution it is very important to study the convergence of the approximation. An extraordinary amount of research has gone into studying the convergence of such numerical solvers. Usually, in time marching problems such as this, one is interested in convergence rates, or how fast the error approach zero when the mesh resolution is increased. In the limits of computing time and power, the formal study of convergence rates was exempt from this thesis, however it was explored using other avenues.

If the same experiment is repeated multiple times and it approaches the same solution, the solver is said to converge. Multiple simulations of the same experiment

were set up and allowed to run for successively longer times. The solution was plotted and visualized intermittently and the results were consistent.

4.3 Results

Given the complexity of the domain shown in Figure 4.1, one could expect an equally complex solution. Fortunately, current efforts suggest that there is an equilibrium solution, which is presented in section 4.3.2. Before this, the development of the flow is discussed with focalized interest on the inlet pipe. An attempt is made to verify the numerical solution in the inlet region with theoretical predictions, namely the analytical solution for flow through a cylindrical pipe (see Section A.4). The properties of the liquid used in the simulation are arranged in Table 4.2

Table 4.2: Liquid Properties

Property		Value	Unit
Dynamic Viscosity	(μ)	1.00×10^{-3}	kg m^{-1} s^{-1}
Density	(ρ)	1.0	kg/L
Analyte Mass Diffusivity	(D)	1.0×10^{-9}	m^2/s
Inlet Volumetric Flow Rate	(Q)	0.1	ml/min

4.3.1 Inlet Flow Development

As mentioned in section 4.2, the boundary conditions chosen will send a shock wave through the volume. For this reason it is interesting to study the inlet pipe as the flow normalizes. As seen in Figure 4.4, the velocity starts out with a nearly flat front commonly referred to as "plug flow". Notice that velocity at the edges is zero in agreement with the no-slip condition. As time goes on the flow profile approaches a parabolic shape (Figures 4.5, 4.6). This is exactly the anticipated result. In Section A.4 a viscous fluid is accelerated just like the one in this simulation. Due to opposing shearing forces between "layers" of the fluid, the profile will not stay flat faced, but will reshape to maximize volume transport. For laminar flows, this is a parabola.

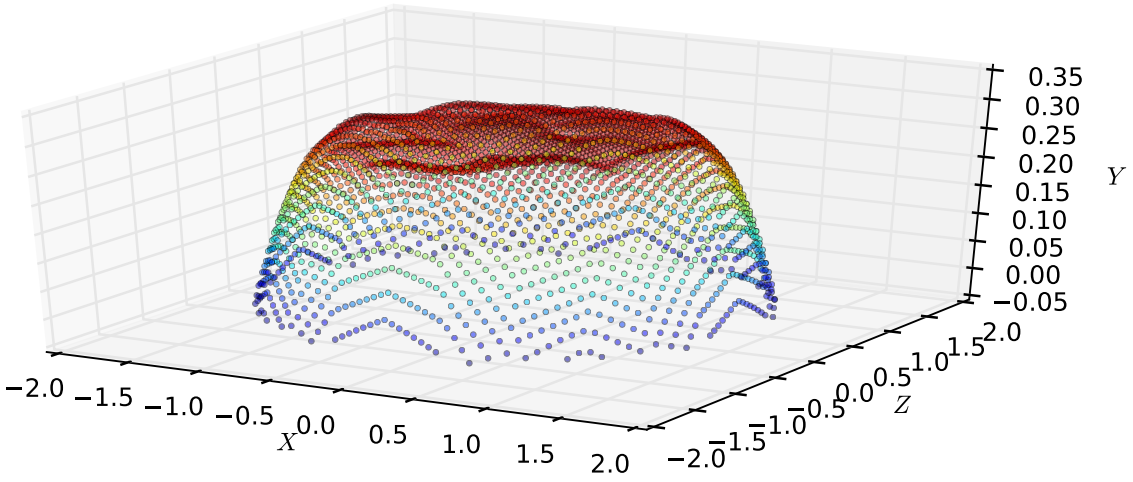

Figure 4.4: Velocity Profile at the Inlet Orifice. $T = 30$ s

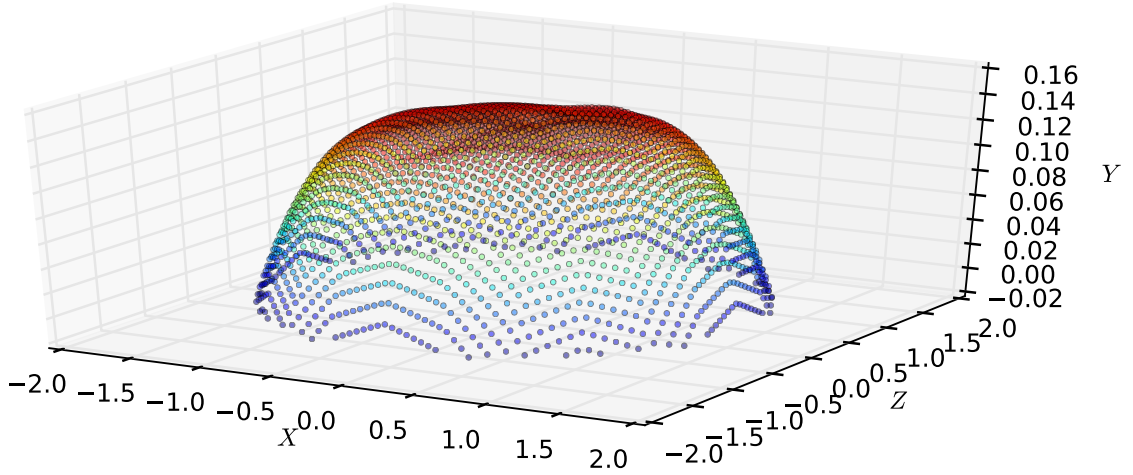

Figure 4.5: Velocity Profile at the Inlet Orifice. $T = 60$ s

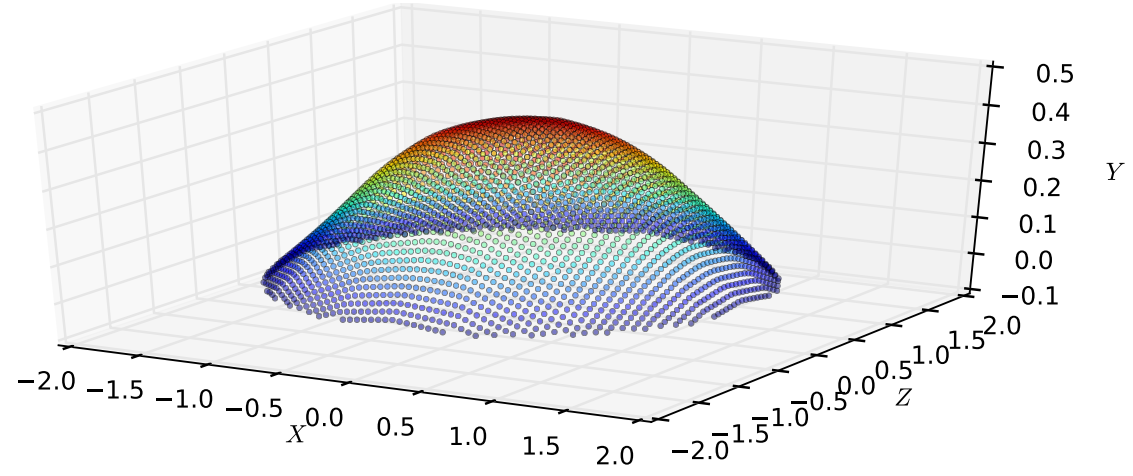

Figure 4.6: Velocity Profile at the Inlet Orifice. $T = 120$ s

Verification of Conservation of Mass

The velocity profile at the outlet is not the same as the inlet, however the volumetric flux at the inlet and outlet is identical at all times due to the incompressibility condition. This was verified by direct integration over the respective surfaces using

$$Q = \int u(R)\, dA, \tag{4.2}$$

however the results are not shown here.

Inlet Velocity Profile

The velocity profile at the inlet is supposedly of the form (Eq. A.6), with a volumetric flow rate given by (Eq. A.7). For convenience the constant $A = -\frac{1}{4\mu}\frac{dp}{dz}$ is introduced as a fitting parameter for the parabolic expression,

$$u(R) = A(a^2 - R^2). \tag{4.3}$$

The flow rate used during typical experiments is 0.1 ml/min or $Q = 100\ \text{mm}^3/\text{min}$. For a pipe of radius $a = 1.587$ mm (Listing 4.1), the parameter A is then:

$$Q = \frac{\pi a^4}{2} A \quad \Longrightarrow \quad A = 0.17\ \text{mm}^{-1}\ \text{s}^{-1}.$$

Since the numerical simulation was carefully manufactured to have the same flow rate, its velocity profile should identically match (Eq. 4.3) with the value of A just calculated. To test the numerical solution, a line was drawn parameterizing R in 1D. The velocity was evaluated and it was indeed parabolic with a fit of $A = 0.18\ \text{mm}^{-1}\ \text{s}^{-1}$ (Figure 4.7). A second exercise, this time parameterizing R in 2D, exploited methods of surface fitting (Figure 4.8) to find that $A = 0.18\ \text{mm}^{-1}\ \text{s}^{-1}$ as well.

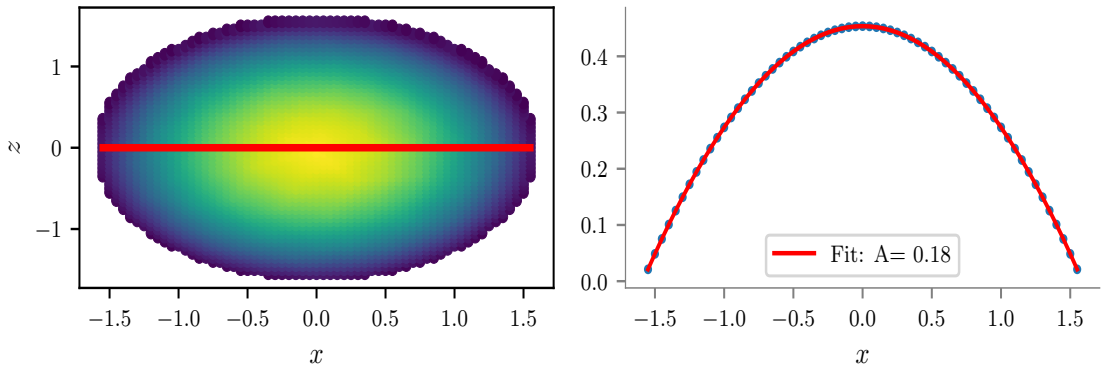

Figure 4.7: The subplot on the left shows a cross section of the velocity profile at the inlet orifice. The color corresponds to velociity magnitude and increases with lightness. The velocity is evaluated at all points on the line bisecting the circle resulting in the profile see in the right subplot. This profile was fit with equation 4.3, and the parameter A was found to be in good agreement with the theoretic result.

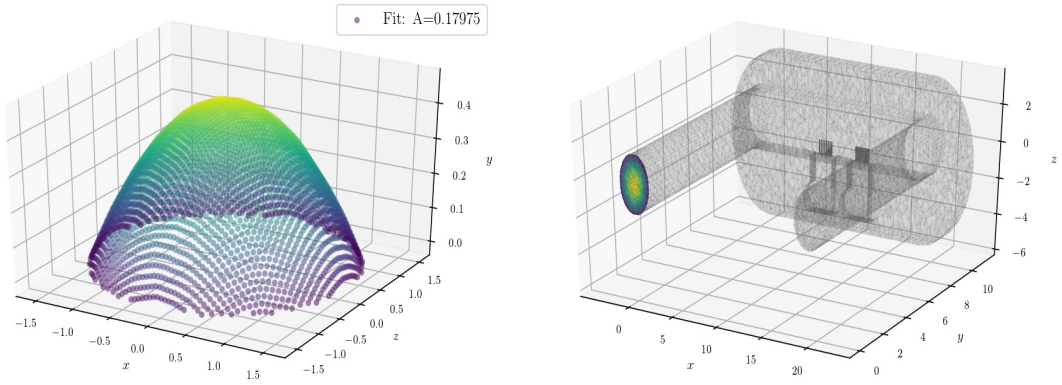

Figure 4.8: The subplot on the left shows a cross section of the velocity profile at the inlet orifice that has been extruded along the pipes axis according to the velocity magnitude. This resulting surface resembles a paraboloid, which was fit with equation 4.3 using surface fittin techniques and the results are in good agreement with theoretical predictions. The subplot on the right show where in the mesh the slice was taken. Both plots use the same colormap, increasing in lightness with velocity magnitude.

4.3.2 Steady State

The velocity and pressure solutions to the Navier-Stokes equations were analyzed throughout the simulation. Eventually, after a 240 s equilibration, the system reached steady state, and all variables became invariant in time. The remainder of this chapter is dedicated to examining the equilibrium solution. This result is very important in understanding actual experimental data. Since detection experiments normally last for a duration much longer than the equilibration time it is reasonable to truncate the early part of the simulation and assume the flow always exists in its stabilized state. This will make things very easy when we later want to introduce chemicals in the system—since the flow is unchanging it is possible to advect chemicals through the medium without needing to simultaneously solve the NS equations.

Figure 4.9 illustrates the velocity profile on a cross section that divides both the inlet and outlet pipe axially through their centres (the $Z = 0$ plane, Figure 4.10). The magnitude of the velocity is indicated by the colorbar, with light areas signifying high velocity. Recall that a fluid will flow through the container in a way that maximizes flow rate. That is, the majority of fluid will flow through light coloured pathways. Vectors are drawn to show the directionality of the flow. The flow appears to follow the general procedure: it starts out moving through the inlet pipe with parabolic velocity profile. Once it reaches the top, the fluid is forced out in all directions. Of course, fluid moving leftwards will not make it very far before colliding with the wall of the container, resulting in a stagnation point— the velocity is nearly zero in this region. The bulk of the fluid moves to the right with an interesting velocity profile (in the region $x \in [2, 8]$ mm). Eventually, the profile becomes uniform ($x \in [10, 17]$ mm) in the vertical direction and resembles the flow between two parallel plates. In order to evacuate the outlet pipe, the fluid must undergo another change in direction, consequently, creating a region of high velocity in the outlet pipe. Unlike the inlet, this profile is not parabolic. For a while, the flow retains a horizontal component to the velocity which causes it to crash into the right side of the pipe. Certain regions of interest will be highlighted later in this chapter.

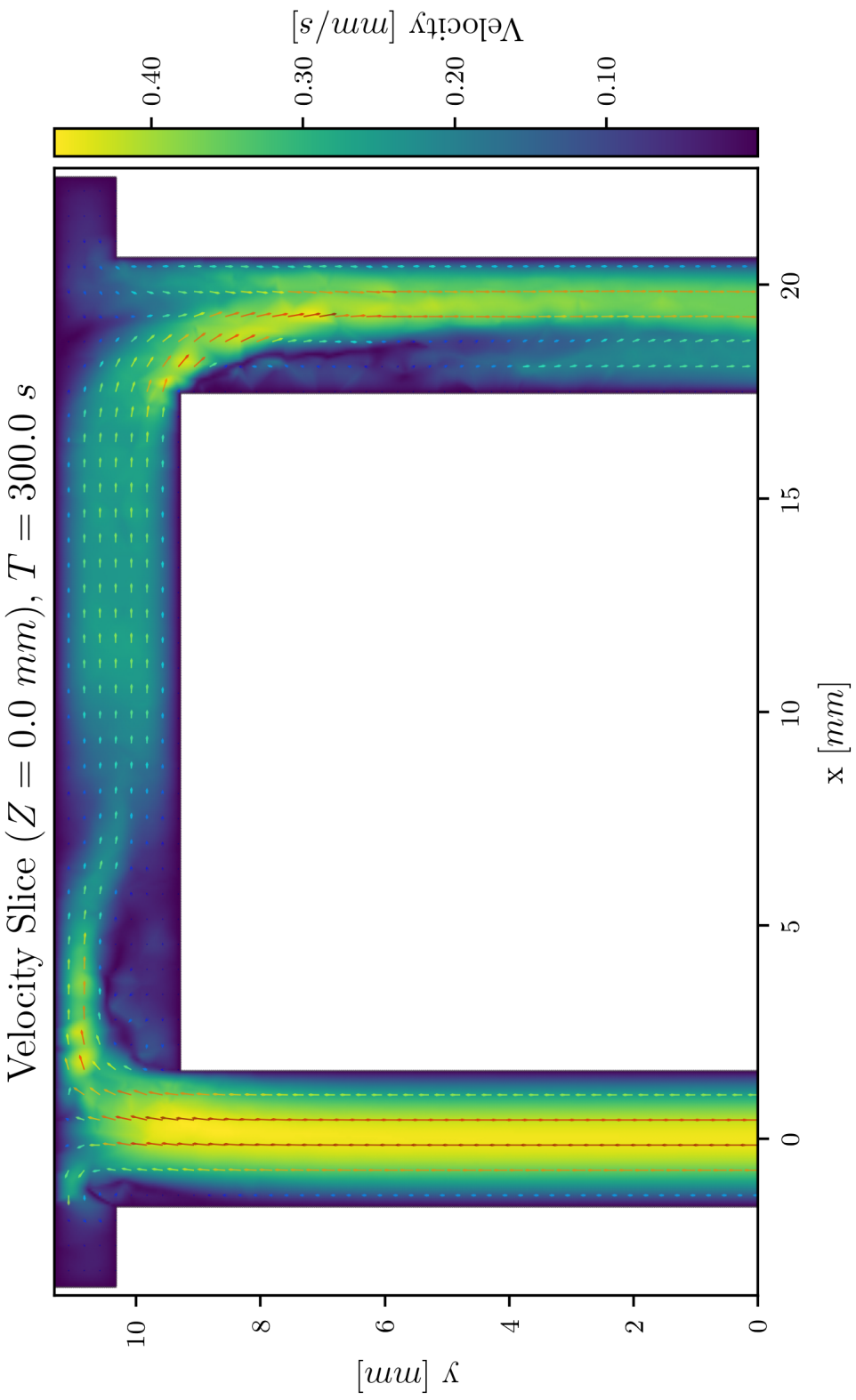

Figure 4.9: Velocity cross section. ($Z = 0.0$ mm, $T = 300.0$ s)

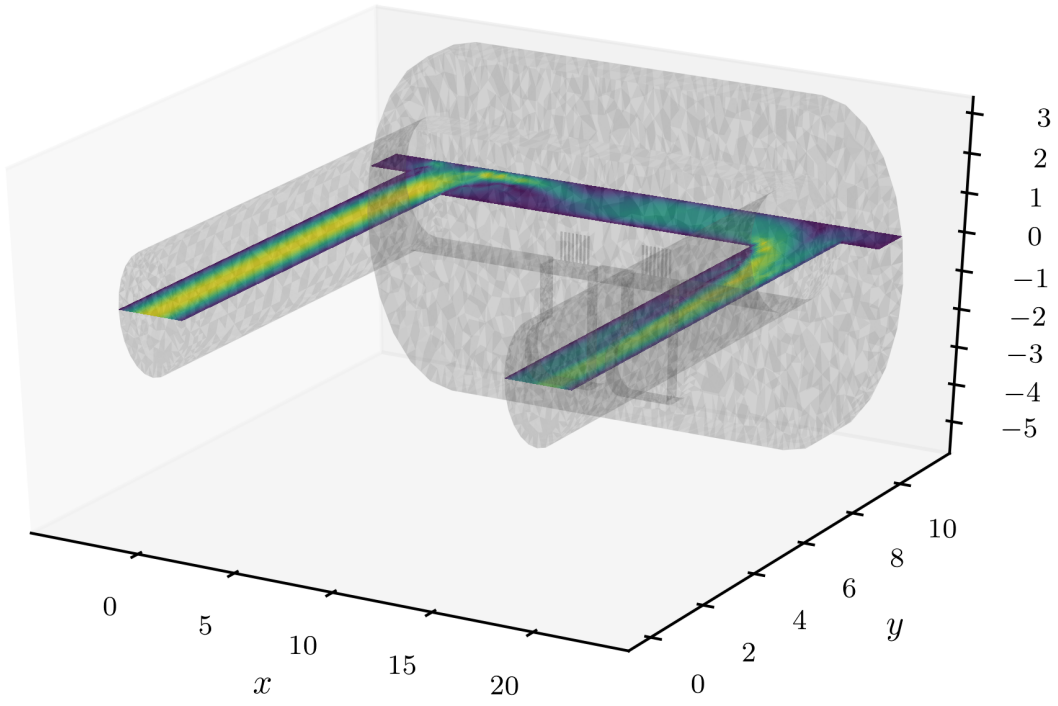

Figure 4.10: 3-dimensional view of the velocity profile showing where the slice was taken. ($Z = 0.0$ mm, $T = 300.0$ s)

The velocity and pressure solutions are complimentary to each other. Notice in Figure 4.11 that the pressure at the inlet and outlet are roughly 0.1 and 0.0 respectively, which was the pressure difference set by boundary conditions to drive the flow. The resulting pressure field has two peculiarities: the high pressure region at the top of the inlet, and the low pressure region at the intersection of the groove with the outlet pipe. Remembering that fluid tends to flow from areas of high pressure to low, helps make sense of Figure 4.9. At the top of the inlet the pressure difference pushes fluid away from the top plate. A top down view of this region is plotted in Figure 4.12.

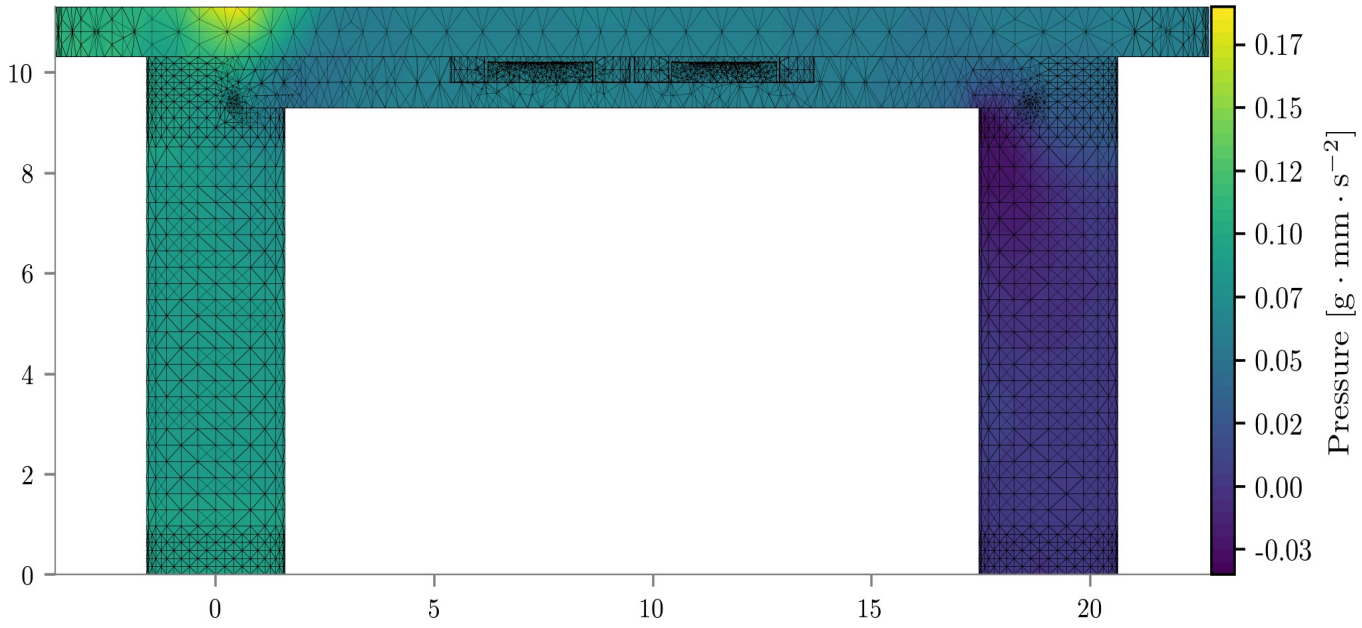

Figure 4.11: Frontal view of the pressure field. ($Z = 0.0$ mm, $T = 300.0$ s)

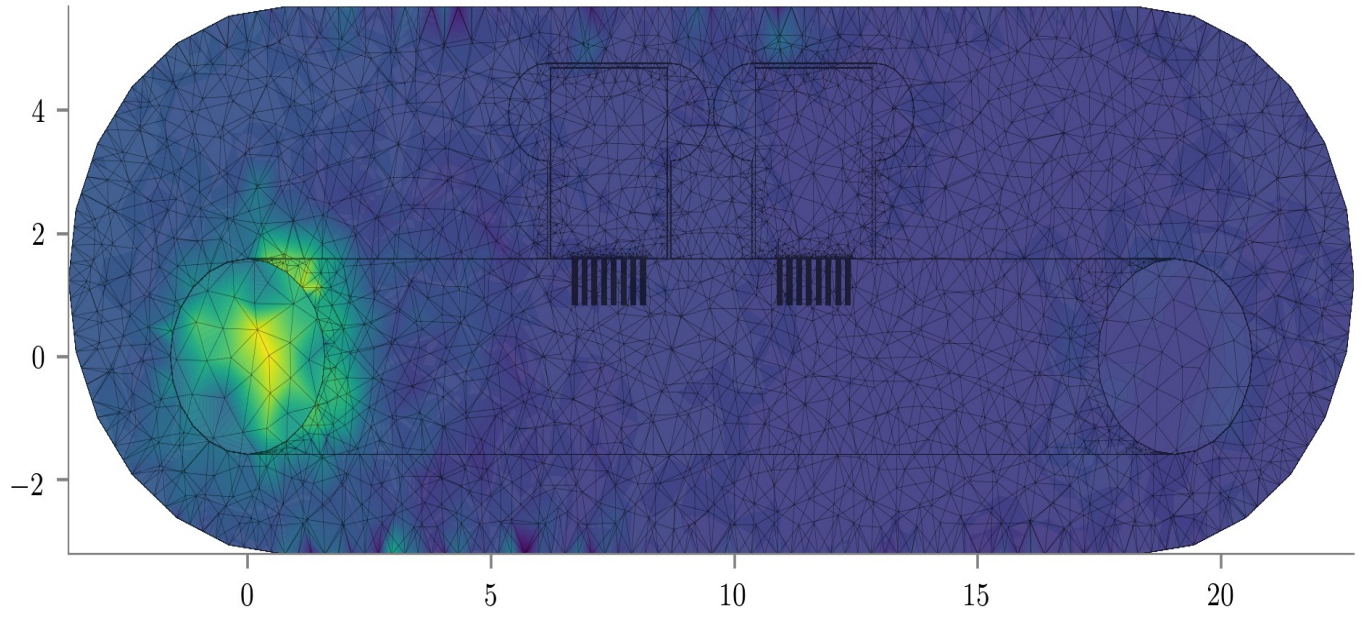

Figure 4.12: Top view of the pressure field. ($T = 300.0$ s)

The velocity profile in the inlet pipe is much different than that of the outlet. Figures 4.13 and 4.14 show magnified views of these regions. Notice in the lower portion of Figure 4.13 that the velocity is directed vertically which maximum at $x = 0$. As it rises in the column it accelerates to the right to make its way around the edge. In doing so, a stagnation point is created in the region between $1 \leq x \leq 2$ and $9.3 \leq y \leq 9.6$.

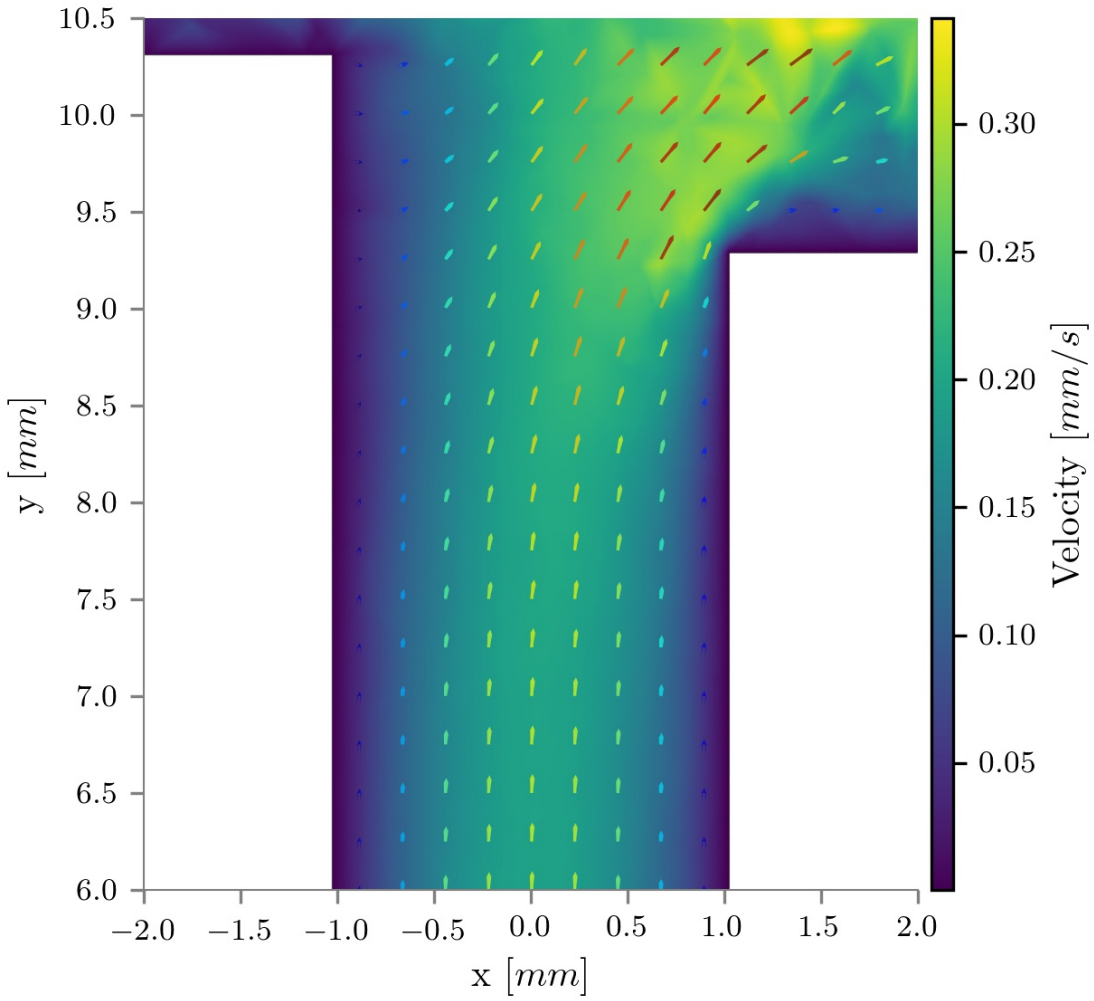

Figure 4.13: Magnified view of the inlet velocity profile. ($Z = 0$ mm, $T = 300$ s)

In contrast to the inlet, the flow in the outlet does not have an axisymmetric velocity profile. Furthermore, the vectors still have a visible horizontal component at $y = 6$ mm (they do at the outlet $y = 0$ mm as well). Much like the inlet pipe, there is a dark region near the edge, indicative of a stagnation point.

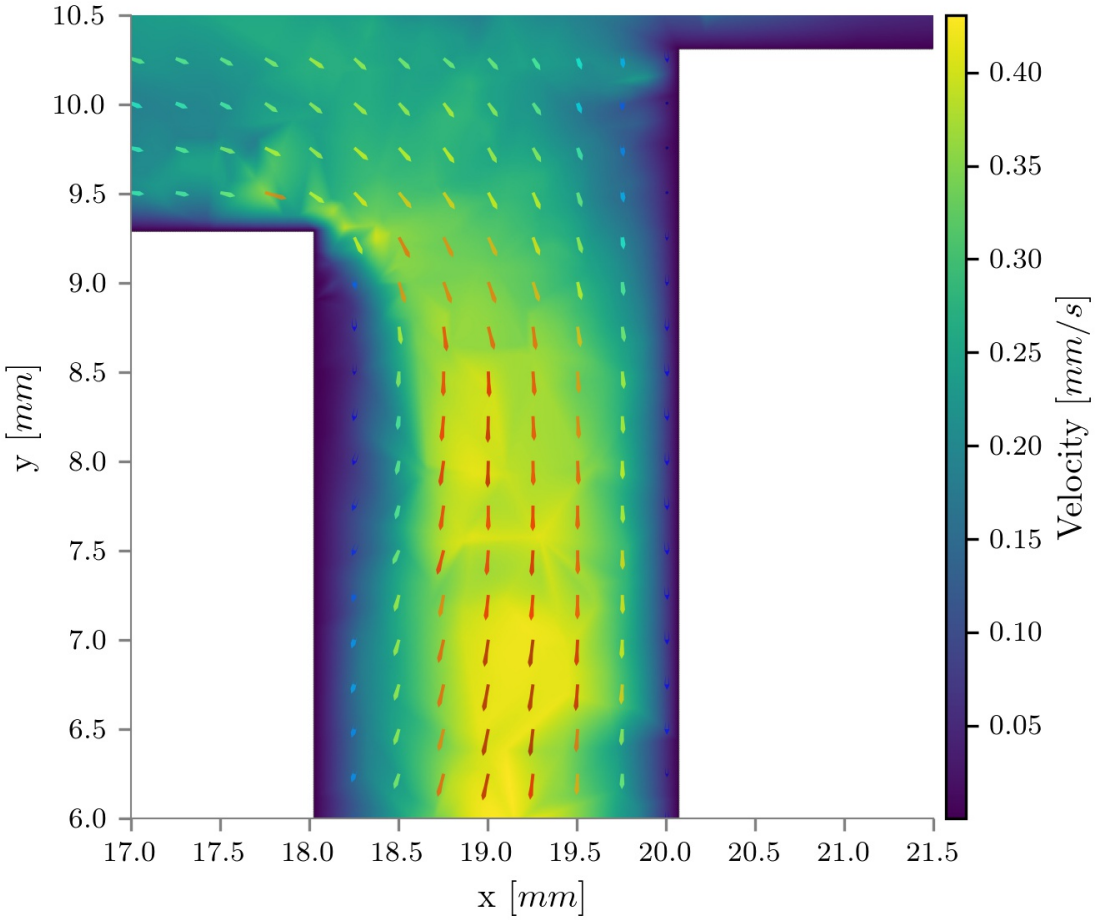

Figure 4.14: Magnified view of the outlet velocity profile. ($Z = 0$ mm, $T = 300$ s)

While there appears to be points of stagnation in the previous figures, a closer examination reveals that there is some fluid motion. Figure 4.15 verifies that the majority of the fluid is moving to the right. However for a small section near the top the fluid is forced to the left. A fluid parcel in this region will follow the vectors which, at least for this particular slice, resembles a circle. In effect, the fluid in this region is trapped, or stagnant.

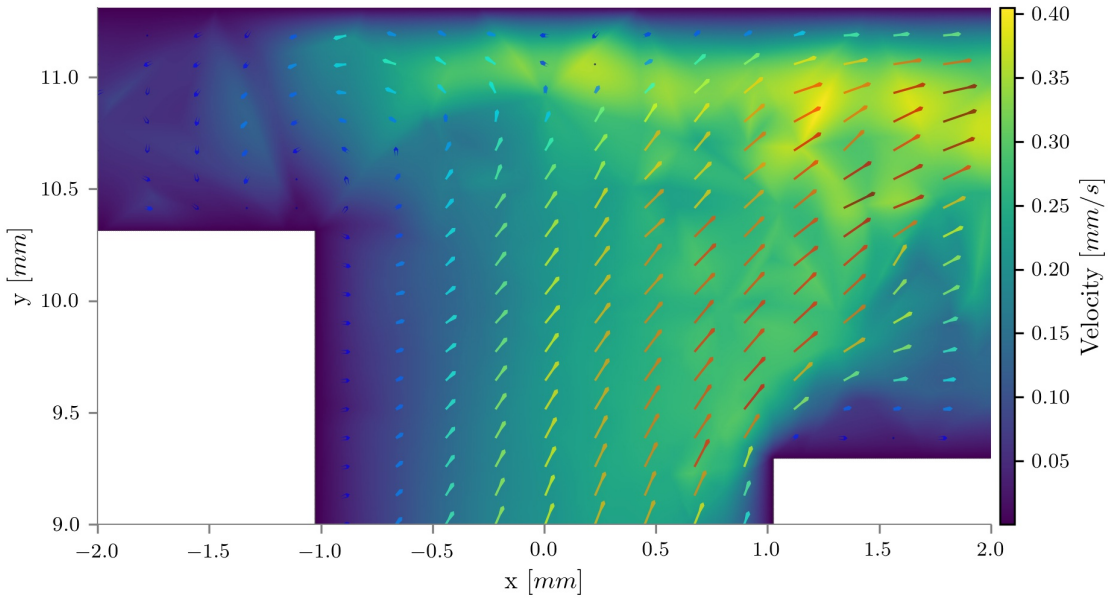

Figure 4.15: Magnified view of the inlet velocity profile near the top of the pipe. ($Z = 0$ mm, $T = 300$ s)

Fluid Flow Around the Cantilevers

The whole purpose of this study was to describe the fluid dynamics around the cantilevers. This would not have been possible without identifying their environment in exhaustive detail. Only now, after considering the domain as a whole, is it possible to observe the impact that the geometry of the setup has on individual cantiilevers. Recall that one of the of the objectives identified in section 1.3 concerned with the relative detection of the cantilevers. While the chemical advection problem is not studied in this thesis, a look at the velocity profile (Figure 4.16) gives reason to believe that the relative detection of the cantilevers will be highly dependent on positioning in the cell. In this figure, it is apparent from light coloured regions that the majority of the fluid flows above the cantilevers. At this magnification each individual cantilever is hardly distinguishable. As a whole, each array appears to divert the fluid smoothly around it in the way of stokes flow—no turbulence or vorticies are created.

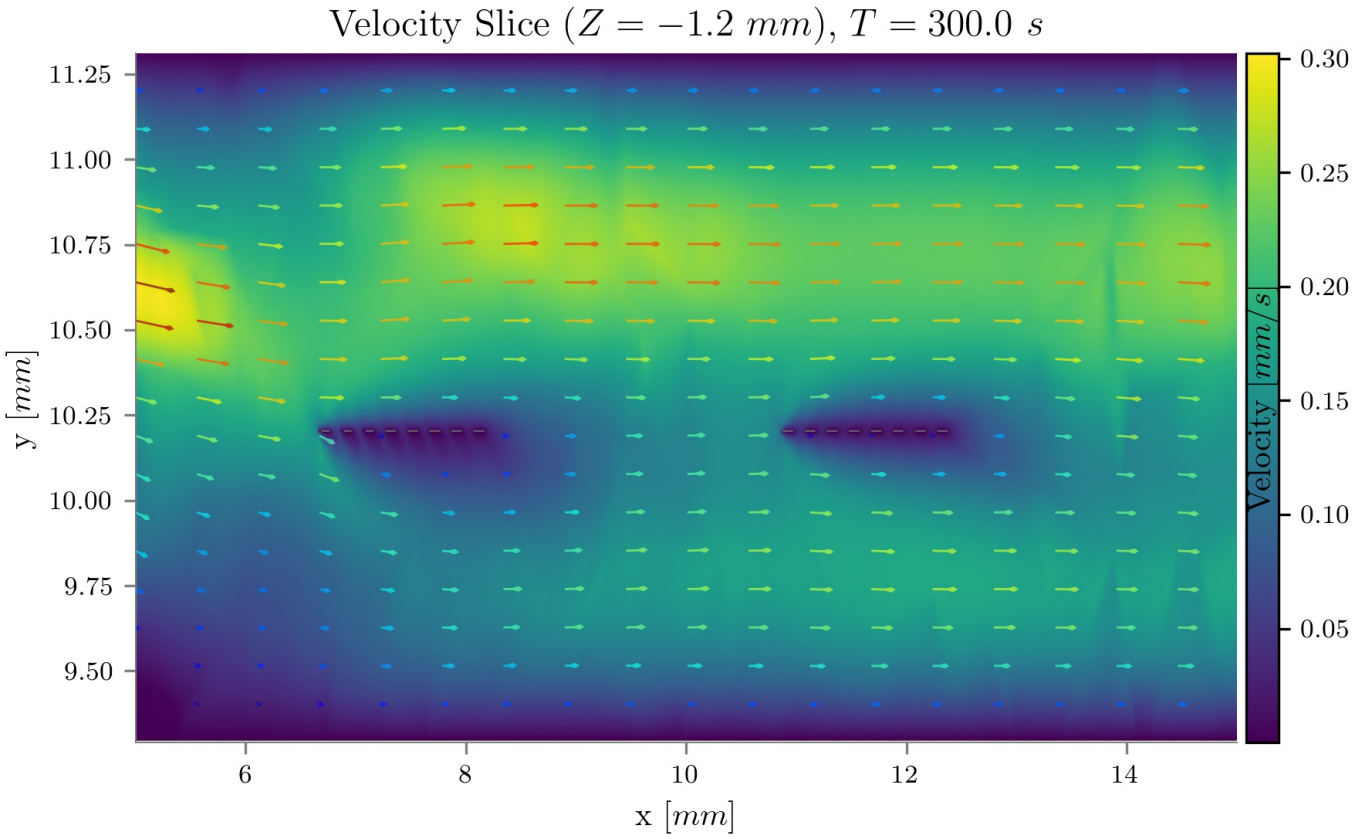

Figure 4.16: Flow around both cantilever arrays. ($Z = -1.2$ mm, $T = 300.0$ s)

A closer inspection of the upstream and downstream cantilever arrays are presented in Figures 4.17 and 4.18 respectively. The main difference between them is the downward velocity over the upstream array. This could have been noticed as early as Figure 4.9, where the fluid is violently forced away from the top of the inlet and down over the cantilevers. Notice that the flow profile is asymmetric across a plane housing the cantilevers ($Y \sim 10.2$ mm) in the upstream array; the dark region on the bottom is not as large on top. On the contrary, the downstream array is nearly a mirror image, confirming that the flow profile is uniform in this region.

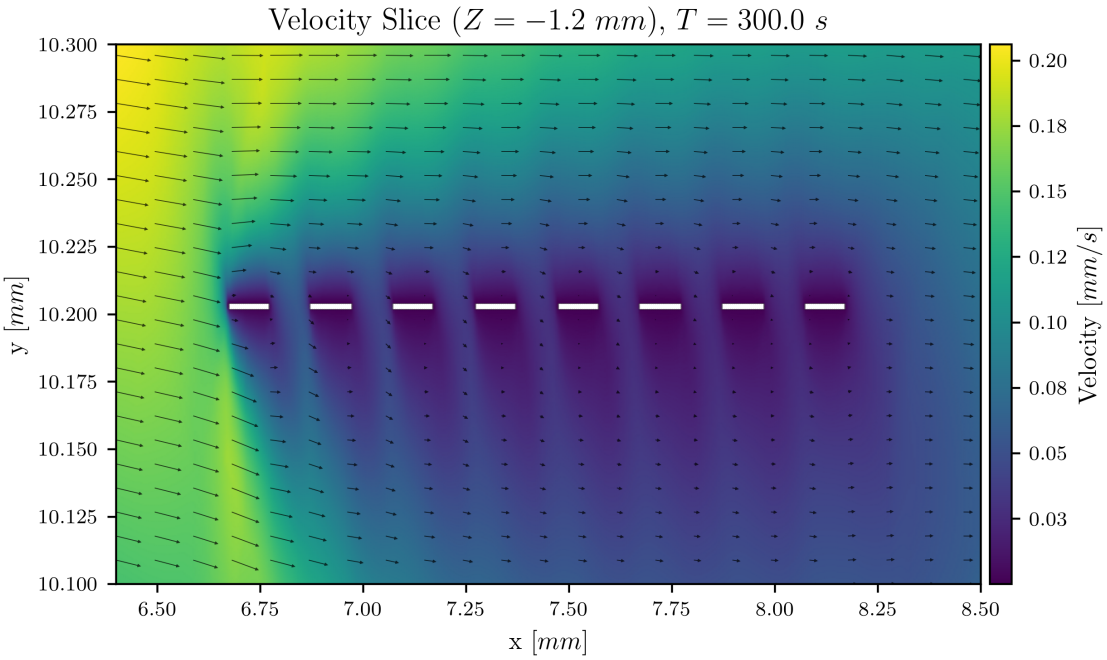

Figure 4.17: Velocity profile in the vicinity of the upstream cantilever array. ($Z = -1.2$ mm, $T = 300.0$ s)

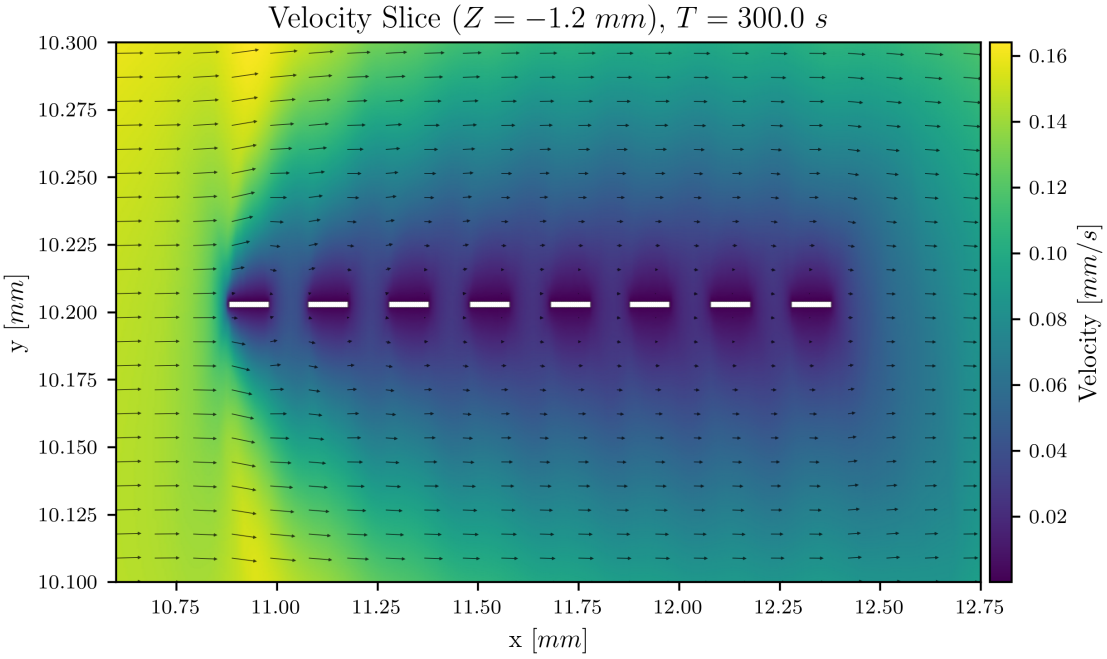

Figure 4.18: Velocity profile in the vicinity of the downstream cantilever array. ($Z = -1.2$ mm, $T = 300.0$ s)

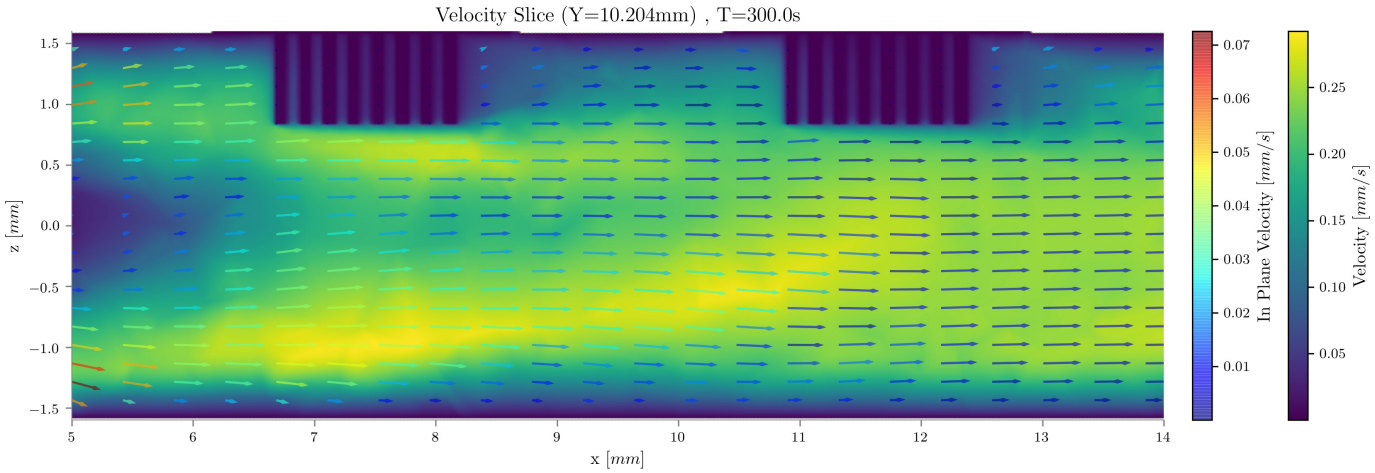

Figure 4.19: Slice of the velocity field showing both cantilever arrays ($Y = 10.204$ mm, $T = 300.0$ s). The 3D velocity magnitude is coloured with light area representing high velocity. The vectors represent the 2D velocity in the plane of the slice, their velocity is indicated by the colorbar.

Figure 4.19 is a cross section of the velocity field with a top down perspective on the cantilevers. The most obvious feature of this picture is the large bright area signifying high velocity magnitude. Realizing that this profile would carry the bulk of the fluid away from the cantilevers (into the bottom stream) and might have adverse effects of the performance of the system- it could inhibit the detection of target particles. While this hypothesis looks clear from the image given, remember that this is a three dimensional problem, and that is just one of the many slice of the data. To tackle this problem correctly requires solving the chemical advection-diffusion equations in 3D.

For the sake of completeness, a slice of the velocity and pressure field in the yz-plane is drawn in Figures 4.20 and 4.21 respectively. This slice was taken at $x = 6.72$ mm, which lies directly over the first cantilever in the upstream array (Figure 4.22). In support of the previous speculation, it appears that the velocity is maximum away from the cantilevers in $x \in [1, 2]$. A slice at second array of cantilevers is not shown here, but it is nearly featureless; the bright area fade away and the vectors reduce in length. The flow gets surprisingly uniform just a few millimetres past the upstream array.

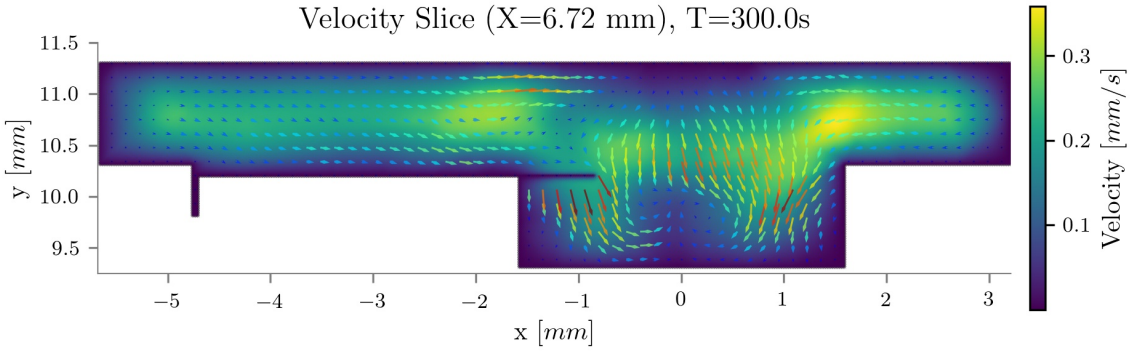

Figure 4.20: Velocity Slice. ($X = 6.72$ mm, $T = 300.0$ s)

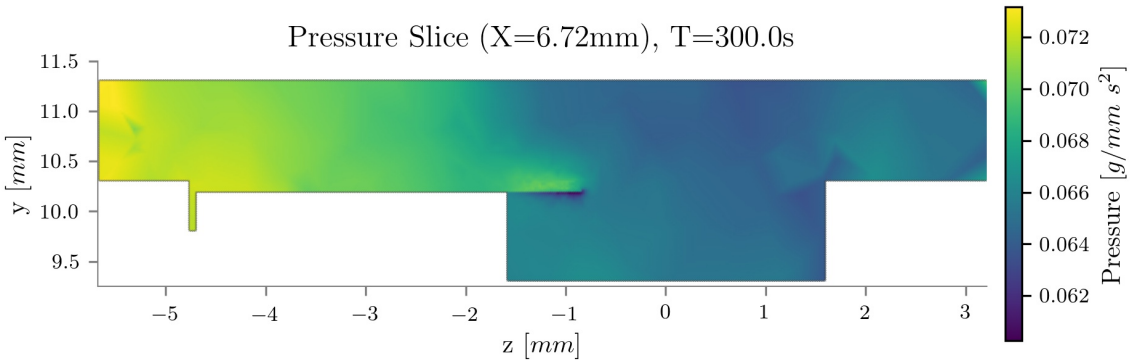

Figure 4.21: Pressure slice. ($X = 6.72$ mm, $T = 300.0$ s)

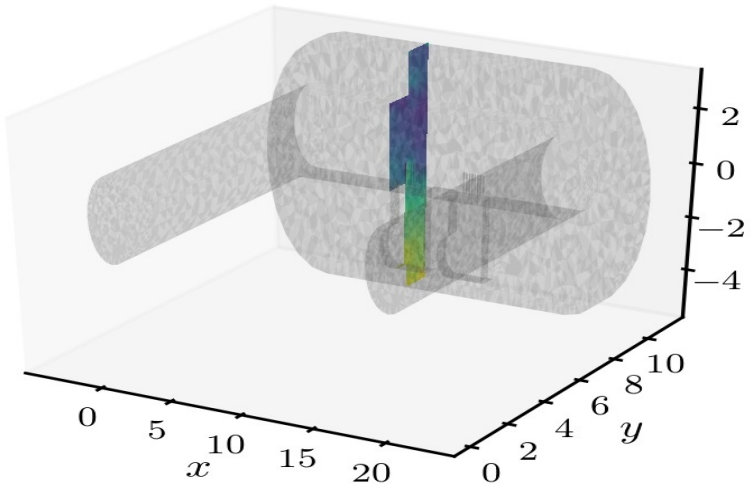

Figure 4.22: 3D view showing where the pressure slice was taken.
($X = 6.72$ mm, $T = 300.0$ s)

Chapter 5

Conclusion

5.1 Summary

Microcantilever sensors are a promising technology for many real life applications. They are able to detect particles in dilute solutions at concentrations as low as 10^{-12} M. While it is possible to obtain a quantitative estimate of the number of target particles adsorbing onto the cantilever's surface based on deflection readings, these numbers have yet to be explained from a theoretical perspective. In this thesis, an attempt was made to model fluid flowing through a microcantilever cell to better understand experimental deflection readings. Initial results show that the flow eventually comes to steady state, with no signs of turbulence, and all of the fluid properties reach an equilibrium. However, the fluids velocity field was not the same around each cantilever. In particular, the array closest to the inlet experienced much more variability in velocity across its top layer. This will likely translate to different deflection readings during actual cantilever sensor experiments. Considering the variations in the fluid flow, it is expected that the concentration of the analyte in solution will vary non-uniformly as well, which could have ramifications on the detection of particles. This model will undoubtedly be a useful asset in future technological developments.

5.2 Future Work

As mentioned on numerous occasions throughout this thesis, solving the Navier-Stokes (NS) equations is only the first step in modelling the experimental setup. The main questions revolve around the adsorption of chemicals onto the cantilever surface. While it was not possible to answer all of the questions listed in the first chapter, the results presented in chapter 4 give them some substantive insight. Now that the fluid motion through the system is known, it can be used to facilitate the much more elaborate chemical advection-diffusion problem. That is, we are in the position to add chemicals to the system, allowing them to advect and diffuse through the fluid, while observing how they distribute throughout the volume. Ideally, the model should be able to monitor exactly how many particles are binding to the cantilevers, thus differentiating the cantilevers from each other. It would be interesting to explore a variety of adsorption models, such as those proposed by Langmuir (I. Langmuir, 1916), to see how well each compliments actual experimental data. There are also many questions surrounding the relative rates of reaction of each cantilever, and the saturation of their receptive layer.

In addition to the chemical problem, it would be nice to see how the fluid itself interacts with the cantilever. Surely, its motion imparts some sort of stress on them. Whether or not this is a significant contributor to the overall deflection remains to be seen. Modelling the elasticity of the silicon cantilevers, taking into account the dynamically changing reactive layer, would be an important problem to tackle.

Appendix A

Supplementary Material

A.1 Lagrangian & Eulerian Reference Frames

There are two ways to describe the kinematics of fluid. First is the Lagrangian description, which monitors a particle of fluid as it travels through the flow field. As in classical mechanics, the Lagrangian is defined to be a scalar function of position and velocity, $f(\mathbf{x}(t), \mathbf{v}(t))$, which is independent of a coordinate system. The advantage of this method is that Newtons laws of motion(and therefore conservation laws) apply directly. However, in order to make use of them one must be able to trace each individual particle in flow, which even for simple geometries, is an exhaustive or impossible task.

Given that fluid is a continuum phenomena, a natural extension would be to study it in larger volumes. This idea effectively gives rise to the second method of describing fluid kinematics: the Eulerian desciption. In this method a control volume is fixed in space, and through it the properties of the fluid are expressed as fields, which are functions of space and time, $f(\mathbf{x}, t)$.

In order to fully describe the trajectory of fluid particles (assuming incompressibility) one needs the pressure $p(\mathbf{x}, t)$ and velocity fields $\vec{\mathbf{v}}(\mathbf{x}, t)$, which are the solutions to Navier-Stokes equations. Note that, while the solutions exist at all points in space, they do not represent the pressure and velocity of individual molecules.

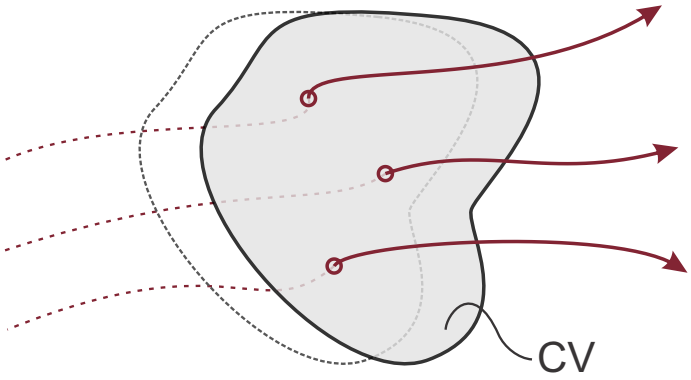

Figure A.1: Control Volume

In many lab experiments, such as the one described in this thesis, fluid is most commonly observed from a stationary reference as in the Eulerian frame, although the mathematics are more conveniently formulated in the Lagrangian frame. Translating between these frames must be done carefully to ensure the validity of Newton's laws. An understanding of both as well as knowledge of the material derivative (section: A.2) is critical in its success.

A.2 Material Derivative

When studying macroscopic material properties, such as temperature or density, one is often interested in how that variable is changing with time. What would be a normal time derivative in a Lagrangian reference frame is more complex from the viewpoint of a stationary Eulerian frame. In addition to monitoring the local changes of the property, one must account for the changing spatial arrangement of the coordinate system. This space-time variation is expressed as a material derivative.

Consider a flow-field property $f(x_1, x_2, x_3, t)$ on a path described by the vector function $\mathbf{x} = \langle X_1(t), X_2(t), X_3(t) \rangle$. The material derivative is:

$$\begin{aligned} \frac{D}{Dt} f(x_1, x_2, x_3, t) &= \frac{\partial f}{\partial t} + \frac{\partial f}{\partial x_1}\frac{dX_1}{dt} + \frac{\partial f}{\partial x_2}\frac{dX_2}{dt} + \frac{\partial f}{\partial x_3}\frac{dX_3}{dt} \\ &= \frac{\partial f}{\partial t} + u_1\frac{\partial f}{\partial x_1} + u_2\frac{\partial f}{\partial x_2} + u_3\frac{\partial f}{\partial x_3} \\ &= \frac{\partial f}{\partial t} + \mathbf{u} \cdot \nabla f \end{aligned} \tag{A.1}$$

where **u** is the velocity of the flow at the fixed position $\mathbf{x} = (x_1, x_2, x_3)$. In an Eulerian description, the material derivative makes it explicit that changes in the variable f are due both to changes in time (as given by the partial derivative) and also the advection of the fluid itself (as given by the dot product with the gradient).

A.3 Surface Forces: Stress Tensor

The stress at any point on a surface can be determined from the stress tensor τ_{ij}. The first index denotes the normal to the surface of interest and the second index is the direction to which it acts. The concept is portrayed pictorially in Figure A.2, where the component vectors of the stress tensor are identified explicitly.

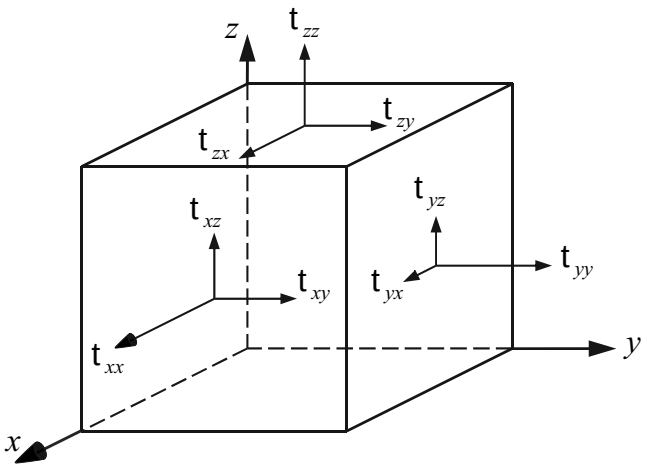

Figure A.2: Stress Tensor Components

$$\tau_{ij} = \begin{pmatrix} \tau_{xx} & \tau_{xy} & \tau_{xz} \\ \tau_{yx} & \tau_{yy} & \tau_{yz} \\ \tau_{zx} & \tau_{zy} & \tau_{zz} \end{pmatrix} \tag{A.2}$$

The stress tensor is symmetric, so that $\tau_{ij} = \tau_{ji}$ [17, p. 63]. This can be justified by considering a infinitesimal volume element ($dV \to 0$) in rotational equilibrium that must conserve angular momentum[7, p. 126].

Consider a cubic volume $dV = dxdydx$ with total area dA. The x-component of the force on the entire surface is

$$dF_x = \tau_{xx}\ dydz + \tau_{yx}\ dxdz + \tau_{zx}\ dxdy,$$

which can be generalized using $d\mathbf{A}_i = \hat{n}_i dA$, for surface normal $\hat{n}$. Dividing by dA gives the force per unit area (traction on a plane)

$$f_i = \sum \tau_{ji} n_j \qquad \text{or} \qquad \mathbf{f} = \hat{\mathbf{n}} \cdot \overleftrightarrow{\tau}. \tag{A.3}$$

An element which is accelerating (changing momentum) will experience a net force on its surface. Provided that the force is reasonably small, and the fluid is Newtonian in nature, then the stress T_{ij} and the strain rate S_{ij} are linearly related. In this regime the imparting stress on opposing sides ($\pm$) of the volume vary by differential amounts. That is, $\tau^+_{xx} = \tau^-_{xx} + \frac{\partial \tau_{xx}}{\partial x} dx$. The net force in the x-direction is

$$dF_x = \left(\frac{\partial \tau_{xx}}{\partial x} dx\right) dydz + \left(\frac{\partial \tau_{yx}}{\partial x} dx\right) dxdz + \left(\frac{\partial \tau_{zx}}{\partial x} dx\right) dxdy.$$

Dividing by the volume $dV = dxdydz$ reveals that this is just the divergence of τ_{ij}. The total surface force per unit volume is

$$\mathbf{f}_{surface} = \nabla \cdot \tau_{ij} \ = \frac{\partial \tau_{ij}}{\partial x_j}. \tag{A.4}$$

A.4 Analytical Solution: Laminar Pipeflow

A closed form analytical solution to the Navier-Stokes equation is known only to exist for a few elementary cases. Among those is the celebrated solution for the flow of an incompressible Newtonian fluid through a cylindrical pipe (Figure A.3). In this problem the flow is driven by an externally applied pressure gradient. The fluid is accelerated until it reaches equilibrium with its resistive viscous forces, at which point the flow profile is said to be fully developed.

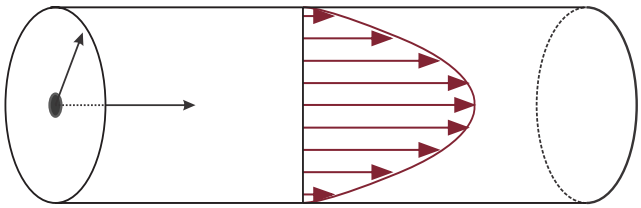

Figure A.3: Cylindrical Pipeflow

Based on the geometry of the problem it is natural to work within the cylindrical coordinate system. Presumably, the velocity profile will be axisymmetric so that

$\vec{u} = \langle 0, 0, u_z(R) \rangle$. Since the components normal to the cylinder axis are zero, the continuity equations $\nabla \cdot u = 0$ is automatically satisfied, and the flow is declared irrotational. The momentum equation (Eq. 2.14), omitting body forces, is restated:

$$\rho \left(\frac{\partial u}{\partial t} + u \cdot \nabla u \right) = -\nabla p + \mu \nabla^2 u.$$

This equation is reduced under the following considerations: u is unchanging along the $\hat{z}$ and $\hat{\phi}$ directions so that $\frac{\partial u}{\partial z} = 0$ and $\frac{\partial u}{\partial \phi} = 0$, and the time derivative vanishes for steady state. Consequently, the differential operators

$$u \cdot \nabla = u_R \frac{\partial}{\partial R} + \frac{u_\phi}{R} \frac{\partial}{\partial \phi} + u_z \frac{\partial}{\partial z} \qquad \text{and} \qquad \nabla^2 = \frac{1}{R} \frac{\partial}{\partial R} \left(R \frac{\partial}{\partial R} \right) + \frac{1}{R^2} \frac{\partial^2}{\partial \phi^2} + \frac{\partial^2}{\partial z^2},$$

simplify the momentum equation in the z-direction to the following:

$$0 = -\frac{dp}{dz} + \frac{\mu}{R} \frac{d}{dR} \left(R \frac{du_z}{dR} \right) \tag{A.5}$$

The conditions mentioned above ($\frac{\partial u}{\partial z} = 0$ and $\frac{\partial u}{\partial \phi} = 0$) reveal that u is a function of R alone. According to (Eq. A.5) p must be a function of z only, therefore the two terms in the equation must be constant to equate. Integrating over R gives:

$$u_z(R) = \frac{R^2}{4\mu} \frac{dp}{dz} + C_1 \ln R + C_2.$$

Logically the velocity cannot be infinite, therefore to avoid the problem at $R = 0$ it must be that $C_1 = 0$. C_2 is found from the no-slip boundary condition $u_z = 0$ at the walls $R = a$. The resulting parabolic velocity distribution is known as Poiseuille flow:

$$u_z(R) = \frac{R^2 - a^2}{4\mu} \frac{dp}{dz}. \tag{A.6}$$

The volumetric flow rate (SI unit: m^3/s) of fluid passing through an area is found by integrating the velocity profile $u(R)$ over that area. For a circular pipe the volumetric flow rate is:

$$Q = \int_0^a u_z(R) 2\pi R \, dR = \frac{-\pi a^4}{8\mu} \frac{dp}{dz}. \tag{A.7}$$

Flow Development

To elaborate, the understanding of flow development is focalized in Figure A.4. Initially, the velocity is constant across the inlet of the pipe due to the immediate action of the pressure gradient. Subsequent motion is opposed by a viscous shearing force. The magnitude of the viscous force varies along the radius of the pipe as a consequence of the no-slip condition. Eventually the velocity profile achieves its optimal volumetric flow rate configuration—a parabola for laminar flows.

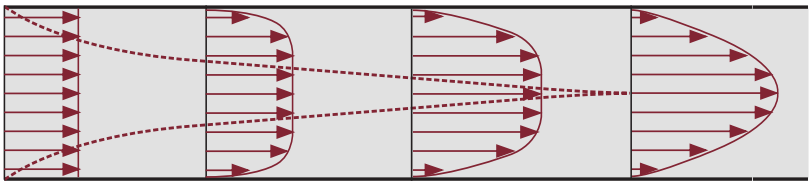

Figure A.4: Developing Flow Profile

Although it is fairly intuitive that the shear stress depends on the radius, the idea can be justified with help of the constitutive relation (Eq. 2.12):

$$\tau_{zR} = \mu \left(\frac{\partial u_R}{\partial z} + \frac{\partial u_z}{\partial R} \right).$$

Using the velocity solution for flow through a cylinder (Eq. A.6) this simplifies to the following, which is a linear function with minimum at $R = 0$ and maximum at $R = a$.

$$\tau = \mu \frac{\partial u_z}{\partial R} = \frac{R}{2} \frac{dp}{dz}. \tag{A.8}$$

Glossary

Dirichlet Condition Specifies the value of the function on a surface, $u(x,t) = f(x,t)$ on $\Gamma_D \subset \partial\Omega$.

Eulerian Specification The understanding of fluid motion from the perspective of a stationary observer who studies how fluid travels through a particular region. A fixed control volume is useful here. See section A.1.

FEniCS A popular open-source computing platform for solving partial differential equations. FEniCS enables users to quickly translate scientific models into efficient finite element code.

GMRES The Generalized Minimal Residual method (GMRES) is an iterative method for the numerical solution of a non-symmetric system of linear equations.

Lagrangian Specification The understanding of fluid motion from observing the trajectory of particles in the flow. A moving control volume is useful in this case. See section A.1.

Neumann Condition Specifies the normal derivative of the function on a surface, $\frac{\partial u}{\partial n} = \nabla u \cdot \hat{n} = f(\mathbf{x},t)$ on $\Gamma_N \subset \partial\Omega$. It is often referred to as a natural boundary condition.

Newtonian Fluid A Newtonian fluid obeys Newton's law of viscosity. There is a linear relation between the stress T_{ij} and the strain rate S_{ij}, which consequently, means that the viscosity is not influenced by forces applied to it. Moreover, a Newtonian fluid is considered to be isotropic, meaning that its intrinsic properties have no preferred direction.

Bibliography

[1] Abdullah Alodhayb. "Development of calix[4]arene-functionalized microcantilever array sensing system for the rapid, sensitive and simultaneous detection of metal ions in aqueous solutions". PhD thesis. Memorial University of Newfoundland, Mar. 2016.

[2] Abdullah Alodhayb. "Towards detecting the human immunodeficiency virus (HIV-1) using microcantilever sensors". MA thesis. Memorial University of Newfoundland, 2011.

[3] J. Anderson. *Computational Fluid Dynamics*. Computational Fluid Dynamics: The Basics with Applications. McGraw-Hill Education, 1995.

[4] K. Goda. "A Multistep Technique with Implicit Difference Schemes for Calculating Two- or Three-Dimensional Cavity Flows". In: *Journal of Computational Physics* 30.1 (Jan. 1979), pp. 76–95. DOI: 10.1016/0021-9991(79)90088-3.

[5] J.L. Guermond, P. Minev, and Jie Shen. "An overview of projection methods for incompressible flows". In: *Computer Methods in Applied Mechanics and Engineering* 195.44 (2006), pp. 6011–6045. DOI: https://doi.org/10.1016/j.cma.2005.10.010.

[6] Victor C. Hayden and Luc Y. Beaulieu. "Modeling Rectangular Cantilevers during Torsion and Deflection for Application to Frictional Force Microscopy". In: *Microscopy and Microanalysis* 15.3 (2009), pp. 259–264. DOI: 10.1017/S1431927609090382.

[7] Pijush K. Kundu, Ira M. Cohen, and David R. Dowling, eds. *Fluid Mechanics*. Sixth Edition. Boston: Academic Press, 2016. DOI: 10.1016/B978-0-12-405935-1.01001-7.

[8] Hans Peter Lang and Christoph Gerber. "Microcantilever Sensors". In: *STM and AFM Studies on (Bio)molecular Systems: Unravelling the Nanoworld*. Springer Berlin Heidelberg, 2008, pp. 1–27. DOI: 10.1007/128_2007_28.

[9] Hans Peter Lang, Martin Hegner, and Christoph Gerber. "Cantilever array sensors". In: *Materials Today* 8.4 (2005), pp. 30–36. DOI: https://doi.org/10.1016/S1369-7021(05)00792-3.

[10] Hans Petter Langtangen and Anders Logg. *Solving PDEs in Python*. Springer, 2017. DOI: 10.1007/978-3-319-52462-7.

[11] Hans Petter Langtangen and Kent-Andre Mardal. *Introduction to Numerical Methods for Variational Problems*. Springer, 2019.

[12] Anders Logg, Kent-Andre Mardal, Garth N. Wells, et al. *Automated Solution of Differential Equations by the Finite Element Method*. Ed. by Anders Logg, Kent-Andre Mardal, and Garth N. Wells. Springer, 2012. DOI: 10.1007/978-3-642-23099-8.

[13] Evangelina Pensa et al. "The Chemistry of the Sulfur–Gold Interface: In Search of a Unified Model". In: *Accounts of Chemical Research* 45.8 (2012), pp. 1183–1192. DOI: 10.1021/ar200260p.

[14] Alfio Quarteroni. *Numerical Models for Differential Problems*. Springer, 2014.

[15] Hang Si. "TetGen, a Delaunay-Based Quality Tetrahedral Mesh Generator". In: *ACM Transactions on Mathematical Software* 41.2 (Apr. 2015), pp. 1–36. DOI: 10.1145/2629697.

[16] Gopikishore Valluru et al. "Synthesis of a cone-conformer bimodal calix[4]arene-crown-5 which forms a sensitive cesium ion sensing layer on gold-coated microcantilevers". In: *New J. Chem.* 38 (12 2014), pp. 5868–5872. DOI: 10.1039/C4NJ01213E.

[17] F.M. White. *Viscous Fluid Flow*. Third Edition. McGraw-Hill Education, 2005.